INSTITUTO SUPERIOR DE ENGENHARIA DE LISBOA

Departamento de Engenharia de Electrónica e Telecomunicações e de Computadores

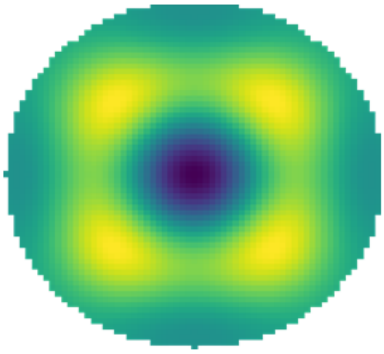

Electrical Impedance Tomography Acquisition System

Fábio Miguel Ricardo da Silva

Licenciado

Dissertação para obtenção do Grau de Mestre
em Engenharia de Electrónica e Telecomunicações

Orientadores : Prof. Doutor Pedro Pinho
Ivan Pombo

Júri:
Presidente: Prof. Doutor António Serrador
Vogais: Prof. Doutor João Costa
Prof. Doutor Pedro Pinho

Dezembro, 2022

INSTITUTO SUPERIOR DE ENGENHARIA DE LISBOA

Departamento de Engenharia de Electrónica e Telecomunicações e de Computadores

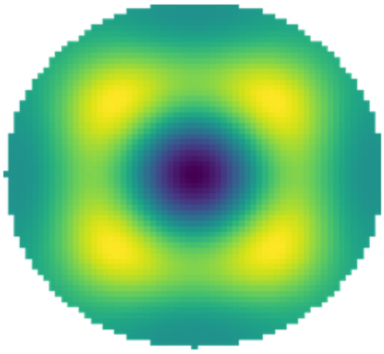

Electrical Impedance Tomography Acquisition System

Fábio Miguel Ricardo da Silva

Licenciado

Dissertação para obtenção do Grau de Mestre
em Engenharia de Electrónica e Telecomunicações

Orientadores : Prof. Doutor Pedro Pinho
Ivan Pombo

Júri:
Presidente: Prof. Doutor António Serrador
Vogais: Prof. Doutor João Costa
Prof. Doutor Pedro Pinho

Dezembro, 2022

To my friends and family …

Acknowledgments

First, I want to thank my advisors, Prof. Pedro Pinho and Ivan Pombo. My special thanks goes to them for allowing me to take on this challenge and for all the knowledge, motivation and critics I was given throughout this phase. All this would not have been possible without their help and support.

I would also like to thank the Instituto de Telecomunicações de Aveiro and its personnel, mainly Paulo Gonçalves, for acquiring the material, fabricating, assembling and helping debug all the boards developed in this work.

To my family, for all the support, incentives and advice I was given. They were present through all my good and bad academic moments. Even in bad moments, they always believed in me, even when I didn't. Words are not enough to explain how grateful I am.

A big thank you to my special friend Francisca for all the kindness and help you have provided since the moment you entered my life. Those late-night calls helped distract me whenever things weren't really going my way as you would always find a way to comfort me and make things better.

Thank you to my friends Miguel, Martim, Rita, Pedro, Marina and Carlos for the friendship developed throughout our academic lives. For all the help, be it in my academic or personal life.

To all those not mentioned here, but that helped in some way in my life so far.

Abstract

Electrical Impedance Tomography (EIT) is a non-invasive medical imaging technique that, from voltage and current measurements taken at the body's frontier, allows the determination of the electrical conductivity from different tissues inside the body. Since each tissue presents distinct electrical conductivity values, it is possible to form a medical image.

In this method, some factors should be considered, for example, the number of electrodes supported and the excitation pattern used. An increase in the number of electrodes allows for an increase in spatial resolution. Another characteristic is the implication different measurement frequencies have in the produced medical image.

In this dissertation, a low-cost prototype with a capacity for 32 electrodes to acquire these signals was developed. This new prototype allows measurements starting at 1 kHz up to 100 kHz, with a fixed current amplitude of 500 µA. To acquire the response, a Programmable Gain Amplifier (PGA) was used, with gains of 1, 10, 100 and 1000 V/V, followed by a 12-bit Analog-to-Digital Converter (ADC) at a sampling rate up to 1 MSPS.

To validate the system a few medical images were produced and presented in this dissertation, namely of a human arm, a phantom used for Microwave Medical Imaging and, finally, a water tank with different objects placed inside.

Keywords: Electrical Impedance Tomography, conductivity, tissue, Digital Signal Processing

Resumo

A Tomografia de Impedância Elétrica (TIE) é um método de imagem médica não-invasivo que através de medições elétricas na fronteira de um corpo, tensão e corrente, permite determinar as condutividades elétricas dos diferentes tecidos presentes no interior do corpo. Uma vez que cada tecido tem uma condutividade elétrica distinta é possível, então, formar uma imagem médica.

Neste método, alguns fatores deverão ser considerados tais como o número de elétrodos suportados e o seu padrão de excitação. Com o aumento do número de elétrodos consegue-se obter uma imagem com maior resolução espacial. Outra característica é perceber qual a implicação de se utilizarem elétrodos com frequências distintas.

Nesta dissertação de mestrado foi desenvolvido um protótipo, de baixo custo e com capacidade para 32 eléctrodos, para aquisição destes sinais. Este protótipo permite efetuar medições desde 1 kHz até aos 100 kHz, com uma amplitude de corrente fixa de 500 µA. Para a aquisição da resposta foi utilizado um amplificador programável com ganhos de 1, 10, 100 e 1000 V/V, seguido de um Conversor Analógico para Digital de 12 bits com uma taxa de amostragem até 1 MSPS.

Para a validação do sistema foram produzidas algumas imagens médicas, apresentadas nesta dissertação, nomeadamente de um braço humano, um fantoma utilizado para técnicas de imagem com microondas e, finalmente, um tanque de água com diferentes objectos colocados no seu interior.

Palavras-chave: Tomografia de Impedância Elétrica, condutividade, tecido, Processamento Digital de Sinal

Contents

List of Figures **xvii**

List of Tables **xix**

Acronyms **xxi**

1 Introduction **1**

- 1.1 Motivation . . . 1
- 1.2 Previously Implemented Prototype . . . 2
- 1.3 Dissertation Goals . . . 3
- 1.4 Document Organization . . . 3

2 System Architecture and State of Art **5**

- 2.1 Basic System Architecture . . . 5
- 2.2 State of Art . . . 10
  - 2.2.1 Thorax Imaging . . . 11
  - 2.2.2 Breast Imaging . . . 13
  - 2.2.3 Continuous Monitoring . . . 15
  - 2.2.4 Brain Imaging . . . 16
  - 2.2.5 Bioimpedance spectrum analysis based systems . . . 17

3 Hardware Implementation 19

3.1 Signal Generator . . . 20

3.1.1 Spectral evaluation . . . 20

3.2 Band-Pass Filter . . . 21

3.2.1 Low-Pass Filter . . . 22

3.2.2 High-Pass Filter . . . 24

3.2.3 Design and Simulation Results . . . 25

3.2.4 Designed Band-Pass Filter Evaluation . . . 26

3.3 Voltage Controlled Current Source . . . 27

3.3.1 Howland Current Source . . . 29

3.3.2 Improved Howland Current Source with buffer circuit . . . 30

3.3.3 Effect of OpAmp Non-Idealities . . . 31

3.3.4 Design and Simulation Results . . . 33

3.3.5 Designed VCCS evaluation . . . 35

3.4 Multiplexing System . . . 36

3.4.1 Multiplexing board on-resistance measurement . . . 36

3.5 Programmable Gain Amplifier . . . 37

3.5.1 Differential and Common-Mode signals . . . 37

3.5.2 Design and Simulation Results . . . 38

3.6 Analog-to-Digital Converter . . . 39

3.6.1 Peak Detector . . . 40

3.6.2 Anti-Aliasing and Charge-Bucket Filter . . . 41

4 Software implementation 43

4.1 Software Flowchart . . . 43

4.2 SPI Protocol . . . 45

4.2.1 SPI Data Transfer and Modes . . . 45

4.2.2 SPI Limitations on the Raspberry Pi . . . 46

4.3 I/Q Demodulation . . . 46

4.3.1 Principle of operation . . . 47

4.3.2 Advantages and Disadvantages . . . 48

5 System Results and Discussion 51

5.1 Result Discussion 51

5.1.1 Resistor Breakout 51

5.1.2 Human Arm Test 55

5.1.3 Breast Phantom 56

5.1.4 Water Tank 59

5.2 Prototype comparison 63

6 Conclusions 65

6.1 Conclusions 65

6.2 Future Work 66

Bibliography 69

List of Figures

1.1 Previous Prototype DAQ View. 2
1.2 Previous Prototype Relay Board: (a) Side View, (b) Top View. 3

2.1 An example of a basic single-source EIT system. 6
2.2 Adjacent drive pattern representation. 7
2.3 Polar drive pattern representation. 7
2.4 Quasi-Polar drive pattern representation. 8
2.5 Cross drive pattern representation. 8
2.6 Trigonometric drive pattern representation (taken from [8]). 9
2.7 The GOE MF II EIT system [15]. 12
2.8 The Wireless EIT system [23]. 13
2.9 The KHU Mark2.5 system [30]. 15

3.1 Final Implemented System Architecture. 19
3.2 Frequency spectrum of the developed AD9837 board. 21
3.3 Generic Sallen-Key Topology. 22
3.4 2^{nd} Order Low-Pass filter response for different Qs. 23
3.5 Band-pass filter based in the Sallen-Key topology. 25
3.6 Designed band-pass simulated filter response. 26
3.7 Designed band-pass measured filter response. 27
3.8 Current Source: (a) Ideal, (b) Real. 27

3.9 Current delivered to a 1 kΩ versus the output resistance. 28
3.10 Howland Current Source. 29
3.11 Improved Howland Current Source with buffer. 30
3.12 Output impedance versus amplifier parameters. 32
3.13 Output current of the designed VCCS for different loads. 33
3.14 Output impedance of the designed VCCS. 34
3.15 AD8253 simulated transfer function. 38
3.16 Implemented high-speed peak detector's schematic. 40
3.17 ADC's charge-bucket filter. 41

4.1 Flowchart of the Proposed Software. 44
4.2 I/Q Demodulator Block Diagram. 46
4.3 I/Q Demodulator Accuracy Error. 48
4.4 I/Q Demodulator Plot. 49

5.1 Developed Resistor Breakout Board. 52
5.2 Total Resistance Measurement: (a) Voltage, (b) Error. 53
5.3 Differential Resistance Measurement: (a) Voltage, (b) Error. 53
5.4 Differential Resistance Precision Test. 54
5.5 Reconstructed Human Arm. 55
5.6 Human Arm Cross-Section (taken from [56]). 56
5.7 Phantom Top View: (a) No plug; (b) Plug placed (taken from [58]). 57
5.8 Phantom Medical Image Produced by the Previous Prototype. . . . 57
5.9 Breast Phantom Imaging: (a) 1 kHz, (b) 10 kHz. 58
5.10 Water Tank Built for Testing. 59
5.11 Bullet Left Imaging: (a) Reference, (b) Reconstruction. 60
5.12 Bullet Top-Left Imaging: (a) Reference, (b) Reconstruction. 60
5.13 Glass Cup Left Imaging Reference. 61
5.14 Glass Cup Left Imaging: (a) 1 kHz, (b) 10 kHz. 61
5.15 Glass Cup Top Imaging Reference. 62
5.16 Glass Cup Top Imaging: (a) 1 kHz, (b) 10 kHz. 62

List of Tables

2.1 Current Drive Pattern Comparison (adapted from [8]). 9

2.2 Comparison of the different EIT systems described. 18

3.1 Band-pass Filter Component Values. 25

3.2 Parameters used for the simulation. 32

3.3 Voltage Controlled Current Source Resistor Values. 33

3.4 Designed VCCS current, in µA, versus output load and frequency. . 35

3.5 Multiplexing board on-resistance measurement, in Ω. 36

3.6 Peak detector component values. 41

4.1 SPI Modes (adapted from [52]). 45

5.1 Expected and Measured Resistor Values, in Ω. 52

5.2 Precision test expected and measured results, in mV. 55

5.3 Comparison between the two prototypes (as of September 2022). . 63

Acronyms

2D	Two Dimension.
3D	Three Dimension.
AC	Alternating Current.
ADC	Analog-to-Digital Converter.
AGC	Automatic Gain Control.
API	Application Programming Interface.
BIS	Bioimpedance Spectrum.
CMRR	Common Mode Rejection Ratio.
CPS	Crosspoint Switch.
CSV	Comma-Separated Values.
CT	Computerized Tomography.
DAC	Digital-to-Analog Converter.
DAQ	Data Acquisition.
DC	Direct Current.
DDS	Direct Digital Synthesis.
DMA	Direct Memory Access.
DSP	Digital Signal Processor.
ECG	Electrocardiogram.
EIT	Electrical Impedance Tomography.
FFT	Fast Fourier Transform.
FIR	Finite Impulse Response.
FPGA	Field Programmable Gate Array.
FPS	Frames per Second.
GBW	Gain-Bandwidth Product.
GPIO	General Purpose Input/Output.

HAL	Hardware Abstraction Layer.
HF	High-Frequency.
I/Q	In-Phase and Quadrature.
IC	Integrated Circuit.
IF	Intermediate Frequency.
IIR	Infinite Impulse Response.
KCL	Kirchhoff's Current Law.
LO	Local Oscillator.
LSB	Least Significant Bit.
MBI	Microwave Breast Imaging.
MRI	Magnetic Resonance Imaging.
NIC	Negative Impedance Converter.
OpAmp	Operational Amplifier.
PCB	Printed Circuit Board.
PGA	Programmable Gain Amplifier.
PLL	Phase-Locked-Loop.
RMS	Root Mean Square.
ROM	Read-Only Memory.
SNR	Signal-to-Noise Ratio.
SoC	System on Chip.
SPI	Serial Peripheral Interface.
SPS	Samples per Second.
USB	Universal Serial Bus.
VCCS	Voltage Controlled Current Source.
VCO	Voltage Controlled Oscillator.
VNA	Vector Network Analyzer.

1

Introduction

This Chapter aims to introduce the motivation behind this dissertation and its end goal, which is the development of a fully functional, low-cost, Electrical Impedance Tomography (EIT) measurement system based on a previously implemented one. This Chapter also presents the document's organization.

1.1 Motivation

The concept of medical imaging is nothing new. In 1895, while studying cathode radiation, Wilhelm Rontgen, a professor of physics, noticed that some materials would react to this radiation by emitting a faint light. A few weeks after his discovery, he managed to take an X-ray of his wife's hand, the first X-ray ever. In 1901, Wilhelm received a Nobel in Physics for his discovery.

Over the years, many new techniques were introduced, which increased the resolution of the medical image allowing for higher accuracy in the medical diagnosis. Some techniques, such as the Computerized Tomography (CT) scan, even allow a three dimensional (3D) reconstruction of the human body by taking a series of images of different slices. Thanks to these advances in the field of medical imaging, the need for exploratory surgeries has decreased and, with them, the risks associated.

Recently, another technique has been investigated as a potential replacement in some applications, that technique being EIT. One advantage EIT presents over other techniques is being radiation-free, making it suitable in cases where the usage of radiation might be a health risk for the patient. Another advantage is it allows the combination of the EIT data with other algorithms to obtain information that would otherwise need different equipment, such as the respiratory rate. However, EIT is very sensitive to noise in the measurements which makes the reconstruction of an image very complex and computationally intensive.

1.2 Previously Implemented Prototype

The previously implemented prototype is based on a Keysight DAQ970A [1], which, as the name implies, is a Data Acquisition (DAQ) System and a Keysight DAQM900A [2], which is a 20 channel solid-state multiplexing add-on for the DAQ970A.

A Raspberry Pi is used to control the DAQ970A (measure the voltage in the different electrodes) and two Arduino Nanos to control the relay-based multiplexing board. The prototype is shown in Figures 1.1, 1.2a and 1.2b.

Figure 1.1: Previous Prototype DAQ View.

Whilst the DAQ970A is well documented, many of this prototype's characteristics are unknown, such as the frequency used for measurements, the injected current amplitude and the voltage measurement pattern, which is assumed to be single-ended based on the results obtained. Another issue is its price. Even though the DAQ970A is a top-grade laboratory instrument, it's overkill for this application making the project's budget unnecessary and unrealistic for replication.

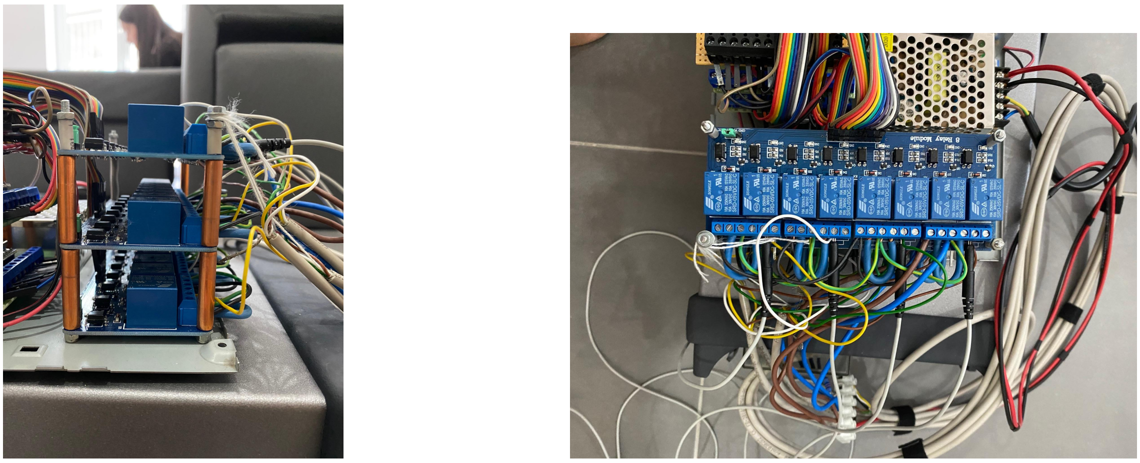

(a) (b)

Figure 1.2: Previous Prototype Relay Board: (a) Side View, (b) Top View.

1.3 Dissertation Goals

The goal of this dissertation is to develop a single-source system for acquiring EIT data. As such, and with the following Chapter in mind, the requirements for this system are as follows:

- A single-source system with a maximum current amplitude of 500 µA, for safety reasons;
- A frequency range from 1 kHz to 100 kHz, at least;
- Compatibility with 32 electrodes for a first phase, scaled up to 64 electrodes in a future phase;
- Software-implemented compatibility with both the adjacent and opposite drive patterns;
- Optionally, software-implemented scripting for arbitrary drive patterns;
- Modular architecture to facilitate future upgrades to each module, i.e. increase the frequency range of the prototype without major architectural changes.

1.4 Document Organization

This document is organized in the following manner. As previously mentioned, Chapter 1 gives a brief introduction to the motivation behind this dissertation as well as the end goal.

In Chapter 2, an explanation of how to construct a basic EIT acquisition system is given. The current excitation patterns are also explored, with their advantages and disadvantages explained. Finally, multiple prototypes were studied, each divided into their final application to understand the relevant parameters of each application.

Chapter 3 presents the hardware development phase of this dissertation, with simulated and practical results, where applicable. This Chapter is divided into Sections, each corresponding to one block of the proposed system's block diagram. Each Section presents reasoning as to why some components were used over others, with some alternatives given.

Chapter 4 presents the software development phase of this dissertation, and since this isn't the focus of the dissertation, this Chapter is kept short. Nonetheless, the Chapter goes over the libraries used and the problems encountered while using the Raspberry Pi platform. The Chapter finishes with a mathematical overview of I/Q demodulation, as this was the technique implemented to obtain the input signal's amplitude.

Chapter 5 presents the results obtained during the testing phase. The Chapter also includes the drawn conclusions from said results, with a critical analysis. The Chapter ends with a comparison between the developed prototype and the previously implemented prototype.

Finally, Chapter 6 presents all the conclusions taken during and after the development phase. The Chapter also presents possible future work to improve the developed system.

In annex to this document are all the final revision schematics of the developed modules.

2

System Architecture and State of Art

Before describing any EIT prototype, it is necessary to have a basic understanding of how they work. As such, this Chapter is divided into two Sections. Section 2.1 presents the two most used architectures, a block diagram of a basic single-source EIT system, the description block-by-block and some fundamentals of EIT systems, i.e, the current drive patterns. Section 2.2 aims to bind the previous Section with the different applications that EIT has been suggested for by presenting a review of the different EIT prototypes currently described in the literature. Divided by their application, these EIT prototypes are compared to each other to understand their most important details and features.

2.1 Basic System Architecture

The current EIT prototypes in the literature present two major architectures, single-source or multiple-source [3]. The single-source architecture uses only one current source and, with the usage of medical-grade multiplexers, it is possible to control multiple channels. As such, these channels are called dependent channels. The multiple-source architecture uses one source for each channel, thus called independent channels. While the single-source architecture has the advantage of using less hardware, since it uses multiplexers to select between electrodes, the latter can make multiple measurements in less time since it is possible to do them in parallel.

A basic single-source EIT system can be broken down into six blocks, as illustrated in Figure 2.1, which presents a block diagram of such a system.

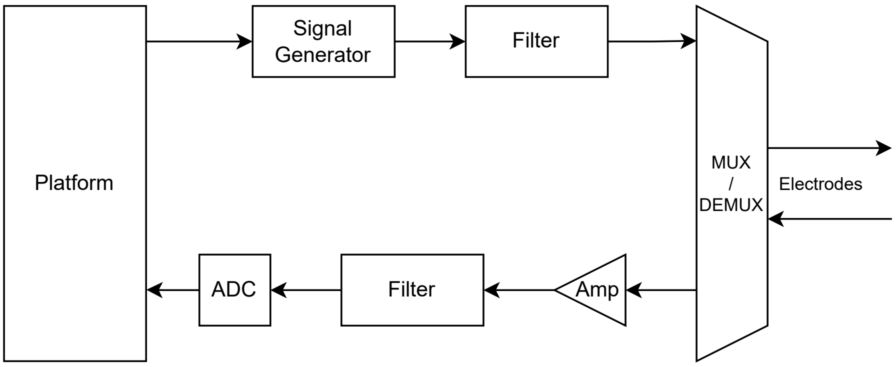

Figure 2.1: An example of a basic single-source EIT system.

Starting with the platform, most recent prototypes use either Digital Signal Processors (DSP) or Field Programmable Gate Arrays (FPGA) since these platforms have high numerical precision. The platform's precision is a concern, as any error in the measurement affects the produced image due to degradation of the Signal-to-Noise Ratio (SNR). Both these platforms also have the advantage of being able to generate a voltage excitation signal for the system, allowing its customization.

The signal generator block can be discrete or continuous. The discrete signal generator usually generates either a signal with a fixed frequency or a signal with multiple frequencies, lowering the overall complexity. However, the latter generates a signal covering an entire spectrum band, for example, a chirp, allowing the analysis in a single sweep. The signal generator output is fed to a Voltage Controlled Current Source (VCCS) as this block outputs a current proportional to the input voltage. This way, it is possible to guarantee that the maximum current injected follows the medical regulations, such as the IEC 60601-1 [4].

The amplifier used to amplify the signal measured between the electrodes needs to feature a high Common Mode Rejection Ratio (CMRR). By featuring a high CMRR, any noise common in both electrodes gets attenuated, reducing the influence in the final image. Before the signal gets digitized by the Analog-to-Digital Converter (ADC), it is possible to introduce a filtering step to remove noise outside the measurement range. The implementation of the filter can be done digitally by using a Finite Impulse Response (FIR) or Infinite Impulse Response (IIR) filter, allowing the change of the filter's response dynamically.

Two considerations also need to be accounted for while designing an EIT prototype, the electrode placement and the drive pattern. While most prototypes usually use a ring of electrodes equispaced for most applications, a few applications might benefit from a different arrangement due to the current distribution and the under analysis object's geometry.

As referenced before, there are various current drive patterns, in an adjacent drive pattern configuration, the current is injected using side-by-side electrodes, as represented in Figure 2.2, and the voltage is measured differentially also between the remaining adjacent electrodes. The current input electrode is called the source electrode, and the current output electrode is the sink electrode [5].

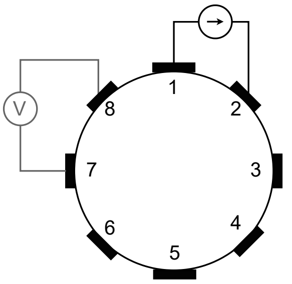

Figure 2.2: Adjacent drive pattern representation.

In a polar drive pattern configuration, the current is injected using two true opposite electrodes, and the voltages are also measured between opposite electrodes, as represented in Figure 2.3. Just like the previous pattern, the current injection electrodes rotate, and the process repeats until all possible pairs of electrodes have been used.

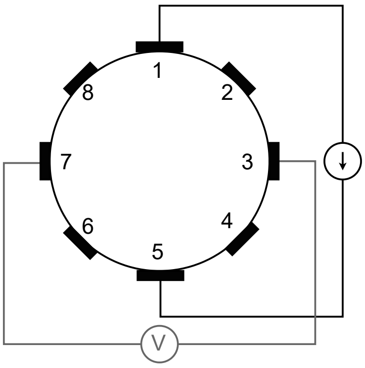

Figure 2.3: Polar drive pattern representation.

In a quasi-polar drive pattern configuration, the current is injected using two almost opposite electrodes, and the voltages are measured between adjacent electrodes, as illustrated in Figure 2.4. The rest of the process is equal to the polar drive pattern and, as such, these two patterns are known as opposite drive patterns.

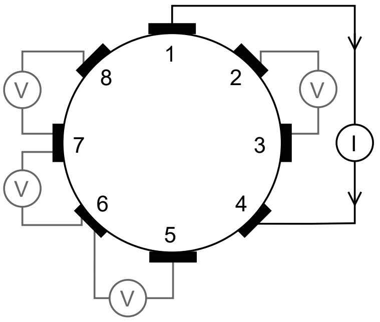

Figure 2.4: Quasi-Polar drive pattern representation.

Another pattern, although uncommon, is the cross drive pattern [6–8]. This technique is more complex than the previous and consists of choosing one current source electrode and a current sink electrode with the same number parity next to it. The voltages are measured adjacently but always skipping one electrode to maintain number parity [7]. Once the measurement is over, the current sink electrode is the new current source electrode and a new current sink electrode is chosen, always maintaining the number parity. Note that this technique is changed between authors in the literature with, for example, [6] defending that the voltage measurement should be done in reference to only one electrode, and [8] defending that there is a two-electrode gap between current injection electrodes. This technique is represented in Figure 2.5, with two measurements to illustrate the electrode placements.

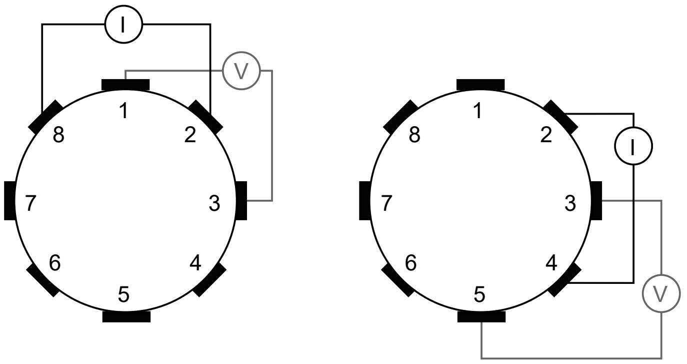

Figure 2.5: Cross drive pattern representation.

The trigonometric drive pattern requires that the system be based on the multiple-source architecture. This current drive pattern uses multiple independent channels to create a uniform current distribution inside the object under measurement by applying different phases to each channel. Figure 2.6 illustrates this current drive pattern, where the red arrows indicate current source electrodes, the green arrows current sink electrodes and the colors inside the electric potential.

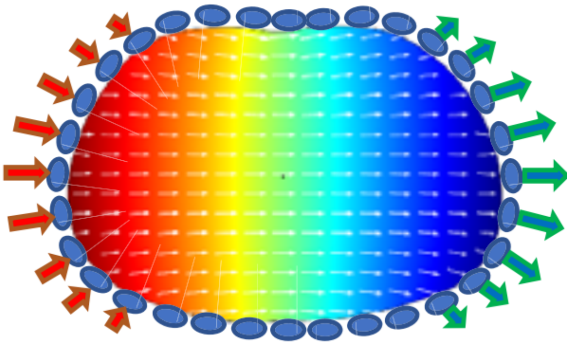

Figure 2.6: Trigonometric drive pattern representation (taken from [8]).

All these techniques produce different types of current distributions, resulting in somewhat different produced images due to their sensitivity. For example, while the adjacent drive pattern has high sensitivity near the outer region since the current distribution is mainly in that region, the cross drive pattern presents high sensitivity near the center due to higher uniform current distribution. Table 2.1 contains a brief comparison between the four current drive patterns described.

Table 2.1: Current Drive Pattern Comparison (adapted from [8]).

Drive Pattern	**Advantage**	**Disadvantage**
Adjacent	Good edge sensitivity	Low center sensitivity
Opposite	Good overall sensitivity	Low edge sensitivity
Cross	Balanced edge and overall sensitivity	Low center sensitivity
Trigonometric	Good edge, center and overall sensitivity	Requirement of a multi-source system

Although these drive patterns were developed for two dimensional (2D) imaging, it is also possible to use them for 3D imaging, with a few drawbacks. As with many medical 3D imaging techniques, such as an Magnetic Resonance Imaging (MRI) or CT Scan, it is possible to use the concept of slicing. By taking multiple 2D images, called slices, of different regions and feeding them into a carefully developed 3D reconstruction algorithm, it is possible to obtain a 3D estimation of the region under analysis. However, due to the current flowing in three dimensions, the 2D slices in EIT will not be as trustworthy as in MRI and CT scanning. A possible improvement in 3D scenarios is to measure the potentials in all layers and not only on the layers where the current is being injected.

To use this technique with EIT, it is necessary to use a layered electrode arrangement, for example, multiple rings of 16 electrodes stacked upon each other. Although this technique works well with non-contact imaging systems, using it with EIT arises another problem since there are spatial limitations as the multiple electrode layers cannot overlap, creating a space with no measurements.

2.2 State of Art

EIT is a novel medical imaging method that basis itself in electrical measurements acquired at the boundary of a region to reconstruct the electrical properties of this region. Contrary to an X-Ray or a CT scan it is radiation-free and enables non-invasive monitoring.

In 1985, Barber, Brown and Seagar established the theoretical aspects of EIT [9]. The method basis itself in determining the conductivity and permittivity distributions of the internal tissues by the application of an electrical current and the potential measurement at the boundary. More specifically, standard electrodes are placed at the surface of the region to image. A low-amplitude electrical current, often in the µA range, is then applied sequentially to the region in consecutive pairs of electrodes or in another pattern, as described previously. Immediately afterwards, the surface potential is measured at the remaining electrodes. These measurements create a voltage profile that allows for the reconstruction of the interior electrical properties.

The problem of determining the internal electrical properties by the surface measurements is non-linear and unstable, i.e., noise in the measurements leads to failure in the reconstruction. Hence, this method does not allow for high spatial resolution like a CT scan or a MRI. However, due to its simplicity and non-harmfulness, it is possible to monitor regions of the body over time. Therefore, the strength of this method lies in the high temporal resolution.

In this Section, a review of the current literature is made to understand how the first EIT prototypes started and further evolved. This Section divides the different EIT prototypes by their applications, ranging from thorax imaging to brain imaging, to understand some aspects of the prototypes, understand which parameters matter the most to which application and what problems and solutions were found.

2.2.1 Thorax Imaging

The diagnosis of different disorders in the cardiac and pulmonary systems might require imaging of the thorax region. There are many techniques nowadays; however, they mostly yield one of two types of information, anatomical or functional information. Anatomical information gives medical staff "a look inside" of the human body with great accuracy, allowing them to see, for example, any deformation of the organs. Functional information, however, allows the medical staff to see how the different organs are operating. Due to these definitions, an important characteristic of the prototypes used is the frames per second (FPS) they can output since, for example, functional imaging requires a high frame-rate. It is necessary to distinguish FPS from measurements per second, as FPS also account for the time it takes for the algorithm to produce an image. Recently, EIT has been suggested as a cheap alternative to image the thorax, with some studies supporting its usage, for example, [10–13].

In 1987, B. H. Brown and A. D. Seagar, from the Sheffield University and Health Authority, described and introduced the first EIT system called "Sheffield Mark 1" or "Sheffield Mk1" [14, 15]. The Mk1 system uses 16 electrodes with a sinusoidal signal at a fixed frequency of 50 kHz and an amplitude of 5 mA peak-to-peak. It uses a single-source architecture, produces 10 FPS, and uses an adjacent drive pattern for the measurements. This system is not able to determine the absolute impedance distribution, being only able to determine relative impedance distributions given a reference image [5].

In 1990, Sheffield University published their second version of the EIT system named "Sheffield Mk2". The successor of the Mk1 now used a fixed frequency of 20 kHz, was able to produce 25 FPS and was mostly digital, unlike his predecessor. Besides these differences, the prototype still used 16 electrodes with an adjacent drive pattern for its measurements [16].

In 1993, a successor to the Mk2 prototype was introduced that brought new features, such as eight different frequencies that the user could choose from, from 9.6 kHz to 1.2 MHz and an adjacent drive pattern for the measurements. The prototype also used what the authors said was incorrectly called [5] triaxial cables to connect to the electrodes to reduce the capacitive coupling between different electrodes. Although the Sheffield Mk3 went back to using analogue technology, like the Mk1 prototype, it achieved a frame-rate of 33 FPS [17].

With [17], Sheffield University introduced their final version of the EIT system so far, the Mk3.5. This system was marketed as Pulmonary Scan Mk3.5 by Maltron

Inc. and had one big difference from the previous prototypes, the number of electrodes used. Due to the disadvantage pointed out by the authors, even though a higher number of electrodes can help obtain higher resolution images, the placement of 16 electrodes was not practical since this prototype was designed for neonatal use. As such, the prototype presents only eight electrodes, with an adjacent drive pattern and 30 frequencies ranging from 2 kHz to 1.6 MHz at a frame-rate of 25 FPS [17] with an SNR of 40 dB [3]. All these devices described only measure the real part of the voltage to simplify the reconstruction process, ignoring the imaginary part.

In the mid-90s, the research group represented by G. Hellige and G. Hahn developed an EIT system, the GOE MF II represented in Figure 2.7. The system operates similarly to the Sheffield Mk2, is digital and uses 16 electrodes with an adjacent drive pattern for measurements [15]. Although many of the device's characteristics are unknown, [18–20] reference that the prototype can operate with a frequency of 50, 75 and 100 kHz, respectively, and [21, 22] refers that the frame-rate of this device is, typically, 13 FPS.

Figure 2.7: The GOE MF II EIT system [15].

One advantage of these systems is the small form factors they can present, making them suitable for telemedicine applications by adding some way to communicate with a backend server. For example, in [23], the authors present a small form factor EIT system with wireless capabilities based on the single-source architecture, which they called Wireless EIT, represented in Figure 2.8.

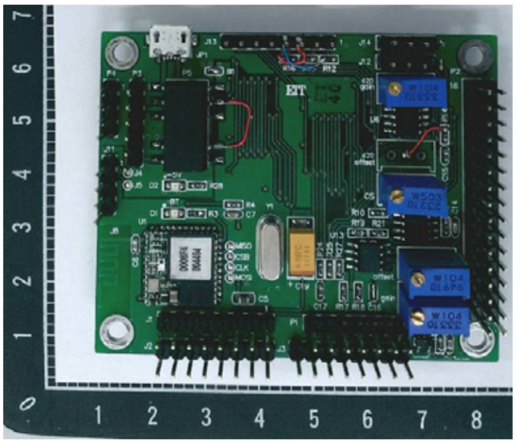

Figure 2.8: The Wireless EIT system [23].

The developed system presents various similarities to the prototypes previously cited, such as 16 electrodes with an adjacent drive pattern and a frequency range from 10 to 200 kHz. However, this system presents a complex demodulator, allowing the measurement of the real and imaginary parts of the human body impedance. The developed system features Bluetooth communication back to a computer or mobile device. The authors also mention that a 5 V power bank can power the device, which, paired with its small form factor and Bluetooth capabilities, allows it to be somewhat wearable. Although not suggested by the authors, since the system communicates to another device, it would only be a matter of software engineering to make it work under telemedicine scenarios.

In [24], however, a portable EIT system for telemedicine scenarios is presented. This EIT system includes a 3G modem to send the measured data to a server that does the image reconstruction. Since the image reconstruction is done off-site, the EIT system presents low power consumption, doing up to 80 measurements with two lithium batteries. Similarly to the previous systems, it uses 16 electrodes based on the single-source architecture with an adjacent drive pattern, making it suitable for thorax imaging. Each full-set of electrode measurements takes about 90 seconds to complete.

2.2.2 Breast Imaging

Recently, EIT has been a subject of studies for early breast cancer detection due to results showing that malignant cancer cells present a lower impedance than normal cells [25, 26]. Since early cancer presents a small volume, the devices used for this application need to have a higher spatial resolution and a higher SNR compared to generic EIT systems. As such, devices used for this type of application present a higher number of electrodes, going as far as using 128 electrodes, trading FPS for spatial resolution.

In [27], a 64 electrode EIT system for 3D breast imaging is developed. Since other literature has suggested that higher frequencies may help detect cancer, this system uses frequencies from 10 kHz to 10 MHz. The system presents an SNR of 90 dB up to 7 MHz, dropping to 65 dB at about 10 MHz and a frame-rate of at least 30 FPS, allowing real-time imaging. Furthermore, the system is capable of measuring both real and imaginary parts of the impedance. The system is modular, with each module containing two identical DSP-driven FPGA-based dual-channel circuits. This way, it is possible to expand the system in the future, if needed. A study done with 96 women determined that the results obtained with this device are according to the reported values in other literature, as pointed out by the authors of [27].

In [28], a mobile EIT Integrated Circuit (IC) for early breast cancer detection is designed and integrated into a simple brassiere. This system also does 3D imaging, presents 92 electrodes with two electrodes for reference, four fixed measurement frequencies of 100 Hz, 1 kHz, 10 kHz and 100 kHz, and six independent channels for voltage measurement to speed up the measuring process in the low-frequency range. The voltage measurement channel uses an instrumental amplifier with a gain of 18 dB, followed by a Programmable Gain Amplifier (PGA) paired with an Automatic Gain Control (AGC) module and a selectable low-pass filter. The resulting system allows the detection of a 5 mm cancer mass with an SNR of 90 dB; however, a concern arises while measuring at 100 Hz. Since the left breast is closer to the heart, the electrocardiogram (ECG) spectrum might influence the system results as pointed out by [29].

In [29], another EIT IC for early breast cancer detection is proposed, taking [28] as a base. Starting with the possible influence of the ECG on the final results, the authors propose to use an ECG adaptive filter by using a homodyne architecture to down-convert the EIT signal to DC, this way reducing the ADC sampling frequency to just 10 kHz. The authors also propose using an I/Q demodulator to obtain both real and imaginary parts of the impedance, allowing for a more complex algorithm to be used. The proposed IC now only contains three fixed frequencies of 1 kHz, 10 kHz and 100 kHz since, as the authors point out, this range is where the change in impedance of the cancer cells is way larger than normal cells. These changes lower the power consumption from 53.4 mW to just 3.8 mW.

2.2.3 Continuous Monitoring

EIT has received attention for long term monitoring applications since it is non-invasive, doesn't require any type radiation and allows for good temporal resolution. Applications have been suggested that range from bedside monitoring of the thorax region to bleeding detection. The prototypes used for these applications require constant calibration to maintain high stability; otherwise, the SNR decreases, lowering the spatial accuracy. The prototypes also need a high frame-rate to obtain information in real-time and allow a fast response, if needed.

In [30], a 16-channel EIT system for long-term monitoring, called KHU Mk2.5, is described. This system includes an automatic self-calibration to maintain a high SNR during long measuring periods. It is based on the multiple-source architecture, which means that every electrode has a dedicated channel since there is no multiplexer to switch between them. This way, it is possible to measure all electrodes in parallel, allowing for faster measurements. The system is presented in Figure 2.9.

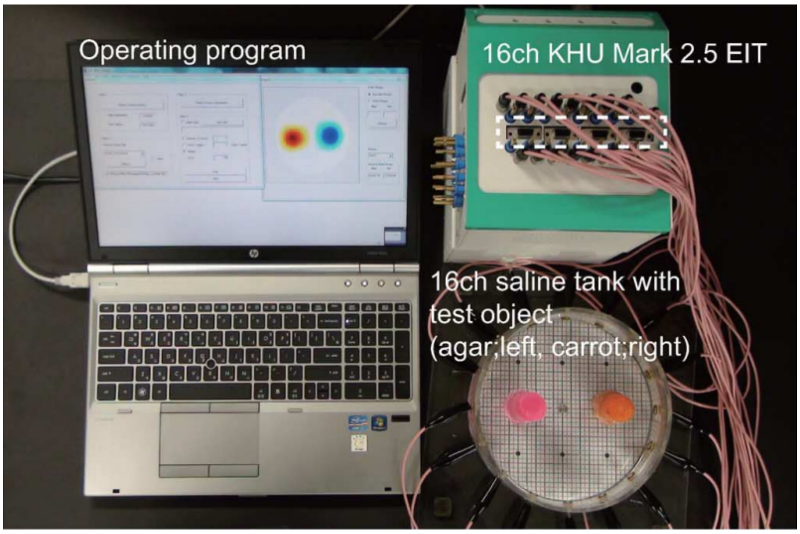

Figure 2.9: The KHU Mark2.5 system [30].

Introducing the self-calibrating system allowed the SNR to stay above 80 dB for frequencies up to 250 kHz during 24 hours of continuous operation. The authors also explain the importance of a high SNR during continuous monitoring, i.e. detecting internal bleedings. Since this system is script-based, the drive pattern can be customized entirely by the user. The frame-rate of this system is 100 FPS at a measuring frequency of 10 kHz, decreasing with lower frequencies (since these frequencies take longer to measure).

In [31], a custom low-power consumption System on Chip (SoC) was introduced for portable lung ventilation monitoring EIT applications. The developed SoC occupies an area of 5 mm x 5 mm and is integrated into a belt to facilitate its placement since it uses 32 electrodes, making it wearable. The SoC features an I/Q generator and demodulator to measure the real and imaginary parts of the body impedance. The overall system has a frame-rate of up to 20 FPS, making it suitable for real-time monitoring, four fixed frequencies (10, 50, 100 and 200 kHz) and a USB port, allowing the connection, for example, to a tablet. The USB connection paired with its weight of only 57 g and belt integration makes it suitable for portable usage. The system features an average SNR of 56.3 dB.

2.2.4 Brain Imaging

EIT has been a subject of study in the brain imaging scene for many reasons. EIT applications in brain imaging include monitoring the brain under normal conditions or neurological conditions, such as a stroke or an epilepsy attack, to understand the impedance changes. EIT can also detect brain cell swelling or internal bleeding, as cell swelling forces the water to go inside the cells, changing the impedance. One difference between the systems used for brain imaging to the other EIT systems is the drive pattern needed. As referenced before, the drive patterns used is dependent on the system's application, and for 2D brain imaging, it is necessary to have good overall sensitivity. As such, due to its bad performance in the center, the adjacent drive pattern is not recommended [8, 32]. For 3D brain imaging, since the head's geometry can't be approximated to a cylinder, the opposite drive pattern shouldn't be used. This reason forces the system to use a more complex electrode switching system allowing a more complex protocol for 3D reconstruction [32].

In [32], a portable, single-source, 64 electrode system for brain imaging is developed and tested, called UCLH Mark 1b. This system operates on a lower frequency range, from 225 Hz to 77 kHz, because, as the authors point out, lower frequencies produce more impedance changes during brain activity. As pointed out before, this system uses an opposite drive pattern. The principal application of this system is to monitor the impedance changes of the brain during seizures in patients receiving a pre-surgical assessment for epilepsy surgery. This system allows for more than 600 electrode measurements per second, corresponding to 3 FPS using a drive pattern with only 31 electrodes. The system performs better at 10 kHz to 30 kHz with an average SNR higher than 50 dB.

In [33], a multi-source, 64 electrode system for brain imaging is described, called KHU Mark 1. Differently from [32], this system has a frequency range from 10 Hz to 500 kHz, the latter chosen due to its performance. The system employs 64 independent channels, all equipped with a demodulation circuit to measure the signal's real and imaginary components and, like in KHU Mark 2.5, the drive pattern is user-defined. One feature this system presents is the possibility to average the measurements, thus increasing the SNR by decreasing the effect random noise has. By using an averaging number of 64 at a frequency of 50 kHz, the system achieved an SNR of 99 dB after one hour of use. This number decreased to 76 dB after two days of use. Finally, by only using 32 electrodes, the system achieved a maximum frame-rate of 3 FPS.

2.2.5 Bioimpedance spectrum analysis based systems

Bioimpedance spectrum (BIS) analysis is a technique that measures the body's response to an entire frequency range. Usually, this technique makes usage of an extensive frequency range, for example, from 1 kHz to 1 MHz. EIT systems can take advantage of a first frequency range test to detect the best frequency range for measurements, corresponding to the frequency range where the body's response rapidly changes [34]. EIT systems using this technique allow for a more in-depth analysis of the body part under measurement, creating a better medical image.

In [34], the authors describe a 16 electrode EIT system based on BIS analysis, named spectrum-based wideband EIT (SWEIT). This system uses a linear chirp containing all frequencies ranging from 1 kHz to 1.1 MHz, allowing the determination of the body's response in a single measurement. With this response, the system creates a signal composed of four frequencies inside the spectrum of interest and does an EIT measurement. This way, by using the impedance change of the various biological tissues under test to determine the best frequencies for analysis, it is possible to discriminate different tissues with similar electrical properties. This system features an average SNR of 56 dB with good consistency.

To finalize this Chapter, Table 2.2 presents all the previous prototypes in a summarized form, keeping only the most necessary details. It should be noted that many values of SNR are missing as these values only became of interest for more demanding applications. However, for older prototypes, the information found in the literature was either not consistent or from unreliable sources and, as such, they were not presented. In this table, results marked with an asterisk were achieved with a specific setup that doesn't include the full range of the system.

Table 2.2: Comparison of the different EIT systems described.

Name	Electrodes	Frequency Range	Drive Pattern	FPS	SNR	Application	Year
Sheffield Mk1 [14]	16	50 kHz	Adjacent	10	-	Thorax Imaging	1987
Sheffield Mk2 [16]	16	20 kHz	Adjacent	25	-	Thorax Imaging	1994
Sheffield Mk3 [17]	16	9.6 kHz - 1.2 MHz	Adjacent	33	-	Thorax Imaging	2001
Sheffield Mk3.5 [17]	8	2 kHz - 1.6 MHz	Adjacent	25	40 dB	Thorax Imaging	2001
GOE-MF II	16	50 kHz - 100 kHz	Adjacent	13	-	Thorax Imaging	1990s
Wireless EIT [23]	16	10 kHz - 200 kHz	Adjacent	-	-	Thorax Imaging	2016
Portable EIT [24]	16	-	Adjacent	-	-	Thorax Imaging	2012
3D EIT System [27]	64	10 kHz - 10 MHz	Trigonometric	30	90 dB	Breast Imaging	2008
EIT IC 1 [28]	92	100 Hz - 100 kHz	Adjacent	-	90 dB	Breast Imaging	2014
EIT IC 2 [29]	92	1 kHz - 100 kHz	Adjacent	-	-	Breast Imaging	2014
KHU Mark 2.5 [30]	16	10 Hz - 500 kHz	Flexible	100	80 dB	Continuous Monitoring	2014
SoC System [31]	32	10 kHz - 200 kHz	Adjacent	20	56.3 dB	Continuous Monitoring	2015
UCLH Mark 1b [32]	64	225 Hz - 77 kHz	Opposite	3*	50 dB	Brain	2002
KHU Mark 1 [33]	64	10 Hz - 500 kHz	Flexible	3*	99 dB	Brain	2007
SWEIT [34]	16	1 kHz - 1.1 MHz	Adjacent	-	56 dB	BIS-based Analysis	2019

As it is possible to observe in Table 2.2, the most common current drive pattern is the adjacent drive pattern. Although it might not be the best one for thorax imaging, since the organs of interest are located in the center region of the body, this was the first one to appear, justifying its usage in earlier prototypes. Its dominance over the many other drive patterns might be influenced by historical reasons and by its simplicity.

In newer prototypes, a trend is seen in their frequency range, going at least from 1 kHz to about 100 kHz, mostly independent of their application. The number of electrodes is completely application-related, with more complex applications using a higher number of electrodes, as is the case of breast and brain imaging, where the spatial resolution is needed to distinguish small masses.

It was also possible to see the evolution in capabilities, with some prototypes using I/Q generators and demodulators to calculate the real and imaginary parts of the body's impedance. Some prototypes even use a heterodyne architecture, which down-converts the measured signal to an Intermediate Frequency (IF), this allows the usage of cheaper, lower-end ADCs with lower sampling rates, which might lower the power consumption of the prototype.

3

Hardware Implementation

In this Chapter, the different implemented hardware modules are described, with simulated and practical results discussed. The final implemented architecture is shown in Figure 3.1, where the dashed arrows represent General Purpose Input/Output (GPIO) connections, the red arrows represent Serial Peripheral Interface (SPI) connections, and the green arrows represent analog signals.

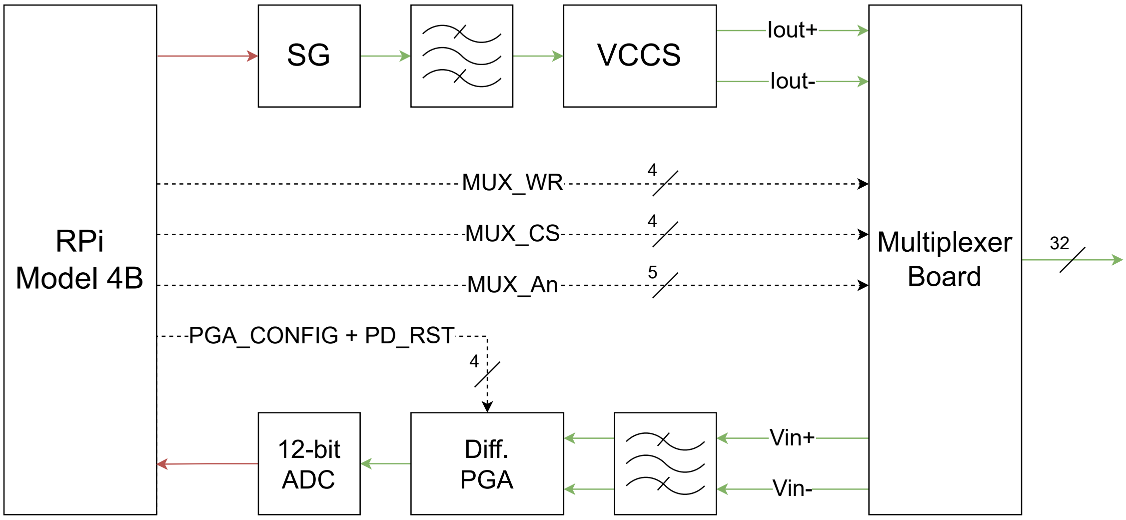

Figure 3.1: Final Implemented System Architecture.

3.1 Signal Generator

As previously mentioned, any EIT system requires a signal generator to generate either one or multiple tones simultaneously. There are many ways to generate a sinusoidal wave. For example, a Voltage Controlled Oscillator (VCO) which, as the name implies, generates a signal with its frequency dependent on the input voltage, can be used; however, as a disadvantage, a Digital-to-Analog Converter (DAC) is necessary. A signal generator can also be implemented by using a Read-Only Memory (ROM) along with a digital clock generator and a DAC. One other way to implement a signal generator is to use Phase-Locked-Loops (PLL) techniques; however, these techniques are usually applied for the generation of very high frequencies.

In this project, a Direct Digital Synthesis (DDS) IC was used. These ICs are a more complex version of a ROM + DAC signal generator, which generate a sinusoidal signal with good frequency resolution, often into the mHz range, due to their digital nature. These ICs are also low-power and require few external components to implement into a system.

The IC used was the AD9837 DDS IC from Analog Devices [35] to generate a tone between 1 kHz and 100 kHz. This IC accepts a master clock input up to 16 MHz, allowing a frequency resolution of 0.06 Hz due to the 28-bit frequency registers present. It communicates with a microcontroller using a SPI-compatible protocol and has a power consumption of 8.5 mW at a power supply voltage of 2.3 V.

3.1.1 Spectral evaluation

An 8-bit, 50 MSPS oscilloscope with a 400k point buffer size was used to measure the spectral content of the signal generator. The oscilloscope's probe was connected to the signal generator's output, with its ground lead connected to the Raspberry Pi's Ethernet chassis for a good grounding point. After the oscilloscope's acquisition, the signal was extracted to a Comma-Separated Values (CSV) file and, with MATLAB, it is possible to filter it and plot the Fast Fourier Transform (FFT) and measure the SNR.

The described procedure can be improved by using a spectrum analyzer to obtain a better spectral response with a lower noise floor; however, most spectrum analyzers don't usually include lower ranges such as 1 kHz. Using an oscilloscope with an averaging function can prove to be beneficial as it averages out any noise not produced by the signal generator IC. Figure 3.2 presents the frequency response obtained.

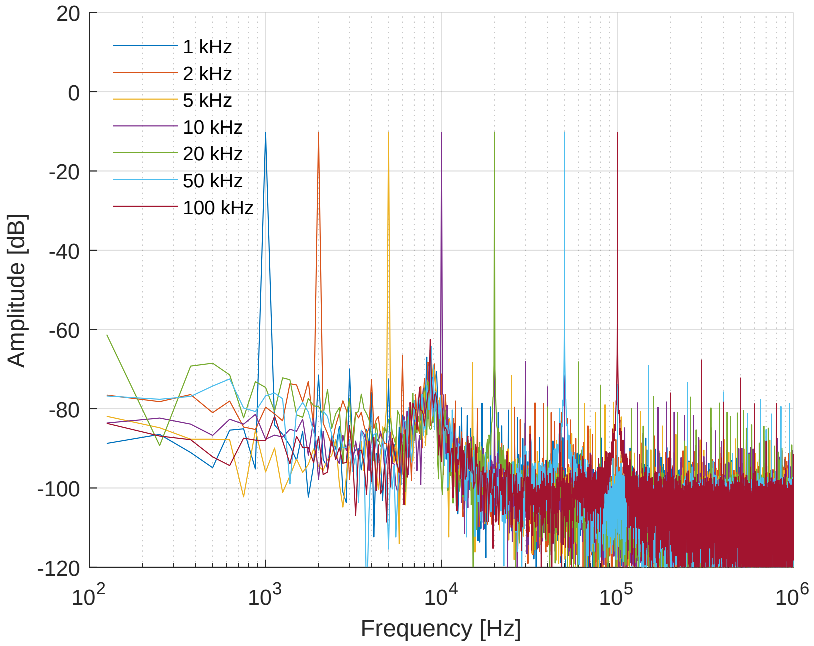

Figure 3.2: Frequency spectrum of the developed AD9837 board.

From Figure 3.2, it is possible to observe that the obtained spectrum is relatively clean, with the signal harmonics being present below -60 dB. The calculated SNR for all frequencies is about 45 dB, from DC to 200 kHz, which is below the specified 65 dB; however, as referred previously, for accurate measurements, a spectrum analyzer is necessary. All the frequency ranges measured present a bump at 8 to 9 kHz caused by the oscilloscope itself, as changing the oscilloscope's time range gets rid of it.

3.2 Band-Pass Filter

As mentioned while presenting the basic architecture of an EIT system, every system must contain some filter to help reduce noise from various sources. For this system, a band-pass filter was implemented by cascading a low-pass filter and a high-pass filter, both based on the Sallen-Key topology, presented in Figure 3.3.

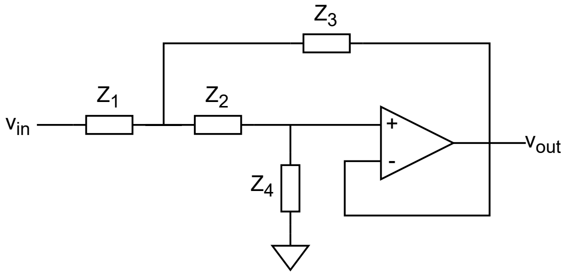

Figure 3.3: Generic Sallen-Key Topology.

Using the Kirchhoff's Current Law (KCL), it is possible to determine the transfer function for this filter; however, since this is a well-known filter, the transfer function is already known to be given by Equation 3.1.

$$\frac{v_{out}}{v_{in}} = \frac{Z_3 Z_4}{Z_1 Z_2 + Z_3(Z_1 + Z_2) + Z_3 Z_4} \tag{3.1}$$

By alternating the different impedances, Z_x, between resistors and capacitors, it is possible to change the filter's response to obtain low-pass, high-pass, band-pass or band-stop filters, keeping in mind that a resistor has an impedance given by Equation 3.2 and a capacitor by Equation 3.3, respectively.

$$Z_R = R \tag{3.2}$$

$$Z_C = \frac{1}{j2\pi f C} = \frac{1}{sC} \tag{3.3}$$

In this arrangement, the OpAmp is used only as a buffer to maintain the filter's response almost independent of the load.

3.2.1 Low-Pass Filter

In order to make a low-pass filter with the topology presented, it is necessary that Z_1 and Z_2 be resistors R_1 and R_2, respectively, Z_3 and Z_4 be capacitors C_1 and C_2, respectively.

By substituting Equation 3.1 with the respective impedances and comparing it with the transfer function of a second-order low-pass filter given by Equation 3.4, it is possible to determine a few parameters.

$$H(s) = \frac{\omega_0^2}{s^2 + 2\alpha s + \omega_0^2} \tag{3.4}$$

Where α is the smoothing factor, used to determine the Q factor, and ω_0 is the cut-off angular frequency given by $2\pi f_0$. The cut-off frequency of the filter is given by Equation 3.5.

$$f_0 = \frac{1}{2\pi\sqrt{R_1 R_2 C_1 C_2}} \tag{3.5}$$

The Q factor of a filter indicates how wide and tall the ringing at the filter's resonant frequency is, typically near f_0. For example, a Butterworth filter presents a flat frequency response with a Q factor of $\frac{1}{\sqrt{2}}$. To further illustrate the impact of the Q factor, Figure 3.4 presents five different filters with the same cut-off frequency but different values of Q.

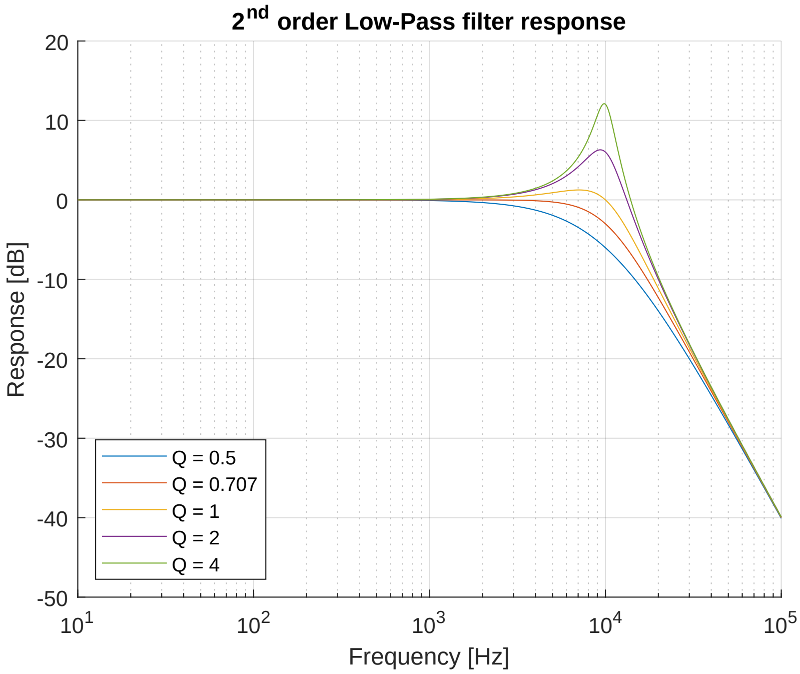

Figure 3.4: 2^{nd} Order Low-Pass filter response for different Qs.

For this filter, the Q factor is given by Equation 3.6.

$$Q = \frac{\omega_0}{2\alpha} = \frac{\sqrt{R_1 R_2 C_1 C_2}}{C_2(R_1 + R_2)} \tag{3.6}$$

To design a low-pass filter, it is necessary to specify the cut-off frequency, f_0, and the Q factor. Since there are four variables (R_1, R_2, C_1 and C_2) for only two parameters, it is necessary to define these variables with ratios of each other, m and n. The approach used in this work was the following:

$$\begin{cases} R_1 = mR \\ R_2 = R/m \\ C_1 = nC \\ C_2 = C/n \end{cases}$$

Where R and C are calculated by setting one of these variables to a fixed value and calculating the remaining using Equation 3.5. By definition, the Q factor is simplified to Equation 3.7.

$$Q = \frac{mn}{m^2 + 1} \tag{3.7}$$

3.2.2 High-Pass Filter

By following a similar approach to the Low-Pass Filter Section, a high-pass filter is obtained by making Z_1 and Z_2 the capacitors C_1 and C_2, respectively, and Z_3 and Z_4 the resistors R_1 and R_2.

Comparing Equation 3.1 with the new impedances substituted with a second-order high-pass filter transfer function, given by Equation 3.8, the same steps can be followed to calculate the cut-off frequency and the Q factor.

$$H(s) = \frac{s^2}{s^2 + 2\alpha + \omega_0^2} \tag{3.8}$$

The Equation 3.5 can be reused to calculate the cut-off frequency; however, the Q factor is now given by Equation 3.9.

$$Q = \frac{\omega_0}{2\alpha} = \frac{\sqrt{R_1 R_2 C_1 C_2}}{R_1(C_1 + C_2)} \tag{3.9}$$

Reusing the same ratios as before, the Q factor is simplified to Equation 3.10.

$$Q = \frac{n}{m(n^2 + 1)} \tag{3.10}$$

By cascading both filters, it is possible to construct a band-pass filter, resulting in the circuit presented in Figure 3.5.

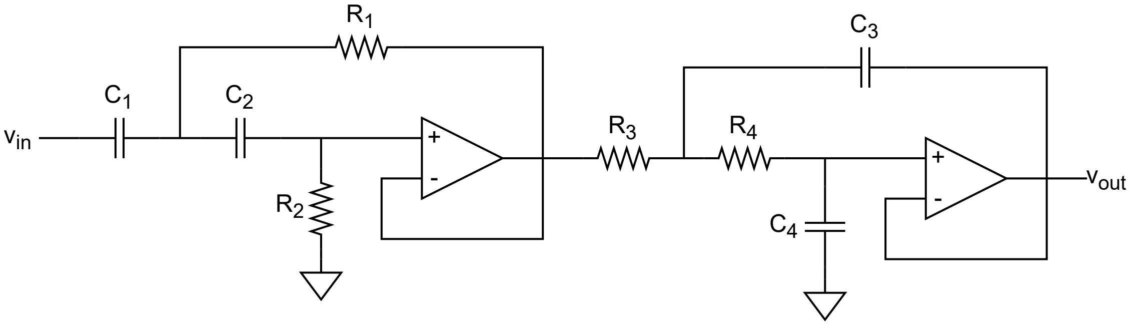

Figure 3.5: Band-pass filter based in the Sallen-Key topology.

Since each filter utilizes a buffer, cascading multiple filters has little to no effect on their characteristics. This way, each filter can be dimensioned individually. In more practical scenarios, the non-idealities OpAmps present limit the filter's isolation from the load, changing its characteristics.

3.2.3 Design and Simulation Results

For this project, a band-pass filter was dimensioned for a band of frequencies starting at 200 Hz and ending at around 200 kHz. This way, the operating frequency band (from 1 kHz to 100 kHz) should pass through the filter without any significant amplitude changes, as the filter's response should be close to 0 dB. The components calculated for the band-pass filter are presented in Table 3.1.

Table 3.1: Band-pass Filter Component Values.

	R1/R3	**R2/R4**	**C1/C3**	**C2/C4**	**Q**	**f_c**
LPF	5.6 kΩ	5.6 kΩ	200 pF	100 pF	0.707	201 kHz
HPF	12 kΩ	22 kΩ	47 nF	47 nF	0.677	209 Hz

Since each filter needs two OpAmps and the measurement/injection is done between two electrodes, a total of four amplifiers are necessary. As such, the LM324PT was chosen since it includes four LM324 OpAmps [36], removing any discrepancies that might exist by using standalone amplifiers ICs.

The band-pass filter was simulated with the component values specified in the previous Table using LTSpice with the LM324 SPICE model offered by Texas Instruments [37]. In Figure 3.6, the acquired filter response is presented in a Bode Plot.

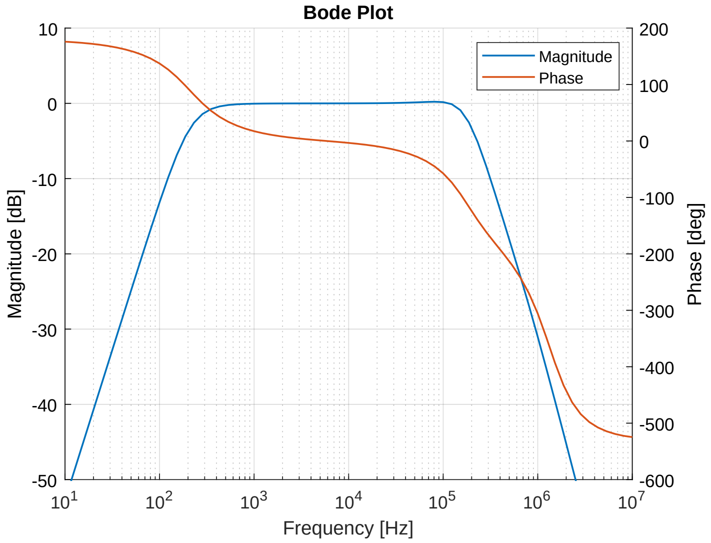

Figure 3.6: Designed band-pass simulated filter response.

Although it is not easy to observe in the previous Figure, the simulated cut-off frequencies are 220 Hz and 196 kHz for the high-pass and low-pass filters, respectively. While it was expected for the low-pass filter to roll off at 40 dB/decade, this does not happen due to LM324's bandwidth which makes the high-pass filter act as a band-pass filter, interfering with the low-pass filter's response. This behavior is more noticeable in the phase, which ideally, would only be from -180° to 180°.

3.2.4 Designed Band-Pass Filter Evaluation

To measure the frequency response of a filter, the 2-port measurement of a Vector Network Analyzer (VNA) is the best tool, in this case, a NanoVNA-H [38]. Since the VNA used has a start frequency of 1 kHz, the frequency response from the high-pass filter cannot be measured. Another option is to use an oscilloscope with bode plot functionality, which allows the measurement of both filters but with lower accuracy.

There are some considerations with the method used since the designed Printed Circuit Board (PCB) uses header connectors for the input signal instead of a standard SMA connector, forcing the usage of an SMA to BNC adapter. Another consideration is the input impedance of the filter, which is not 50 Ω, and, as such, there isn't a match between the VNA and the filter; however, these considerations are more important in higher frequencies. Nonetheless, the results are presented in Figure 3.7, along with the simulated results for comparison.

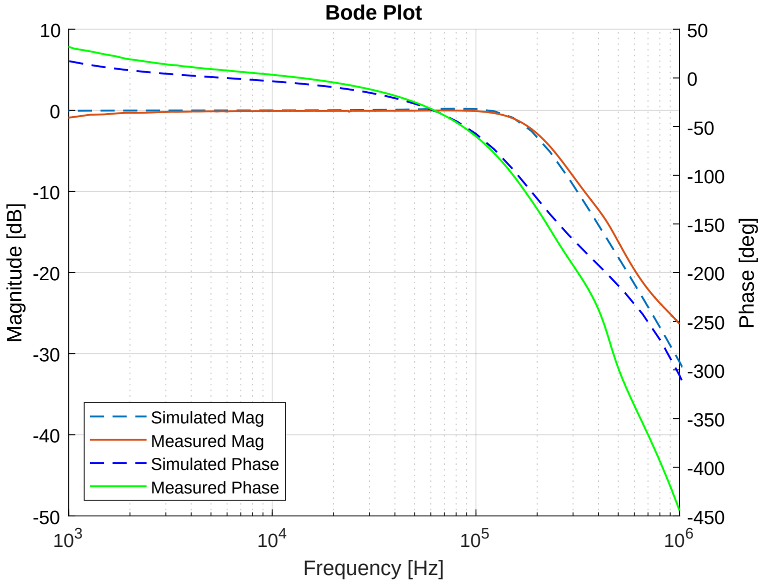

Figure 3.7: Designed band-pass measured filter response.

As it is possible to observe, the measured magnitude of the filter follows the same pattern as the simulated magnitude with some slight deviations at high frequencies (outside the system's measurement frequency range). The measured phase also follows the same pattern as the simulated phase, with a decline at higher frequencies, probably caused by the unaccounted long cables used to connect to the designed PCB. Overall, the designed filter works as intended.

3.3 Voltage Controlled Current Source

The current source of the EIT prototype is one of the most critical blocks. This block is responsible for converting a voltage input, in this case, the output of the signal generator, into a proportional current output to be injected into the electrodes. An ideal current source can be visualized in Figure 3.8a.

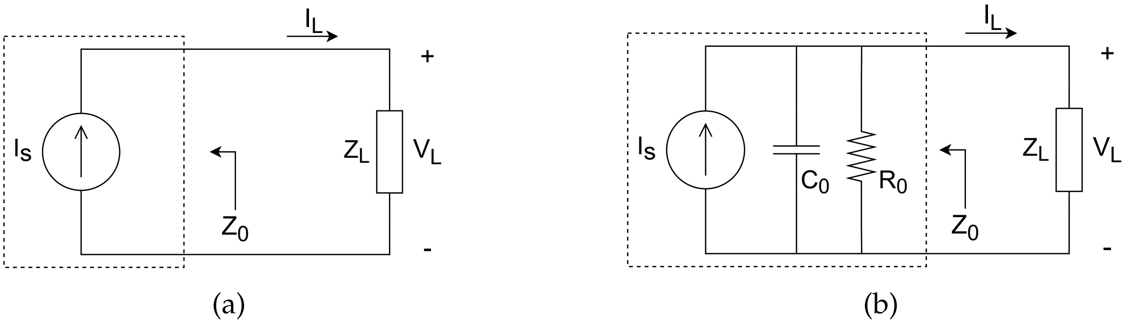

Figure 3.8: Current Source: (a) Ideal, (b) Real.

As the name implies, this current source is ideal, and, as such, the impedance seen from the load (Z_0), also known as the output impedance, is infinite. This way, the total current delivered to the load (I_L) is entirely independent of the load voltage (V_L) meaning that, $I_L = I_S$, [5]. However, this is not the case with real current sources, which present a finite output impedance that is usually composed of the parallel equivalent between a resistance (R_0) and a capacitance (C_0), as it is possible to observe with Figure 3.8b. As such, Equation 3.11 presents the total current delivered to the load.

$$I_L = \frac{Z_0}{Z_0 + Z_L} I_S \tag{3.11}$$

As it is possible to observe with the previous equation, for $I_L \approx I_S$ then $Z_0 \gg Z_L$. To understand the importance of the output impedance versus the current delivered to the load, Figure 3.9 represents a current of 1 mA being delivered to a load of 1 kΩ with the output resistance varying from 1 kΩ to 1 GΩ.

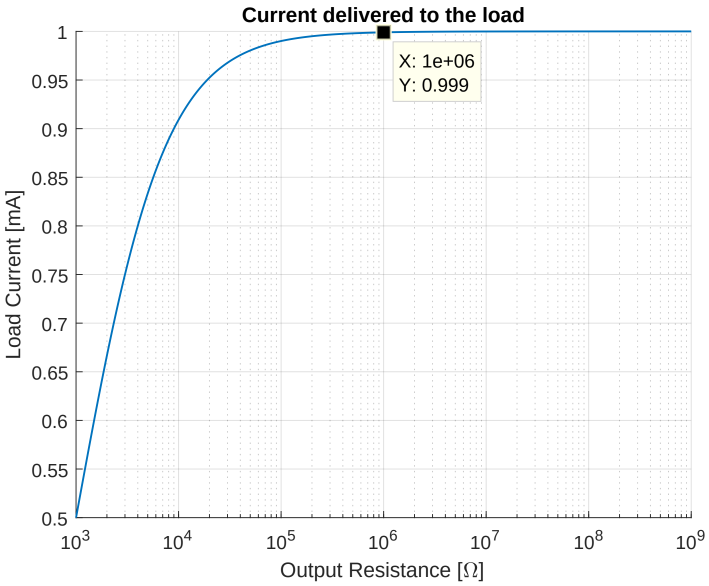

Figure 3.9: Current delivered to a 1 kΩ versus the output resistance.

For this experiment, the output capacitance was ignored, as its influence is determined by the frequency of operation, with higher frequencies shorting the current source. As pointed out in the simulation, an output resistance of 1 MΩ yields a current delivered of about 0.999 mA which equals to an error of 0.1 %, with inferior values rapidly increasing the error.

3.3.1 Howland Current Source

The Howland Current Source, or Howland Current Pump, is a circuit presented in 1962 by Professor Bradford Howland, a professor at MIT. This circuit and its variations are the circuits typically used in EIT prototypes due to their simplicity and high output impedance [39, 40]. The circuit consists of an operational amplifier (OpAmp) and a balanced resistor bridge to form a positive and negative feedback path, as observed in Figure 3.10. This circuit is a grounded-load converter as one of the load's terminals is connected to ground [41].

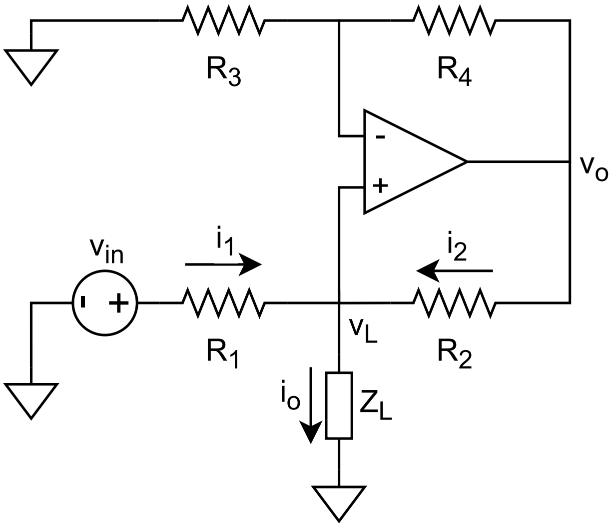

Figure 3.10: Howland Current Source.

To analyze this circuit, basic knowledge of OpAmps, Ohm's Law and KCL is necessary. The amplifier's output v_o is calculated taking into consideration that the amplifier and the negative feedback loop create a non-inverting amplifier with respect to the load's voltage v_L as such, Equation 3.12 can be applied.

$$v_o = \left(1 + \frac{R_4}{R_3}\right) v_L \tag{3.12}$$

By applying the KCL on the load, Equation 3.13 is obtained.

$$i_o = i_1 + i_2 = \frac{v_{in} - v_L}{R_1} + \frac{v_o - v_L}{R_2} \tag{3.13}$$

Combining both equations gives Equation 3.14.

$$i_o = \frac{1}{R_1} v_{in} - \frac{v_L}{R_o} = A v_{in} - \frac{v_L}{R_o} \tag{3.14}$$

The transconductance gain of the circuit, A, is given by the factor $1/R_1$, with units [A/V]. The factor R_o is the circuit's output impedance, given by Equation 3.15, which is the result of the Negative Impedance Converter (NIC) formed by R_2, R_3 and R_4, in parallel with R_1.

$$R_o = \frac{1}{\frac{1}{R_1} + \frac{1}{-R_2R_3/R_3}} = \frac{R_2}{R_2/R_1 - R_4/R_3} \tag{3.15}$$

As previously mentioned, for a true current source, the output current cannot depend on the load's voltage. As such, the condition $R_o = \infty$ must be imposed, known as the balanced-bridge condition, given by Equation 3.16.

$$\frac{R_2}{R_1} = \frac{R_4}{R_3} \tag{3.16}$$

After this condition is met, Equation 3.17 is used to calculate the output current, commonly refereed as the transfer characteristic equation.

$$i_o = Av_{in} \tag{3.17}$$

3.3.2 Improved Howland Current Source with buffer circuit

Two major improvements can be done over the last circuit. The new circuit can be observed in Figure 3.11.

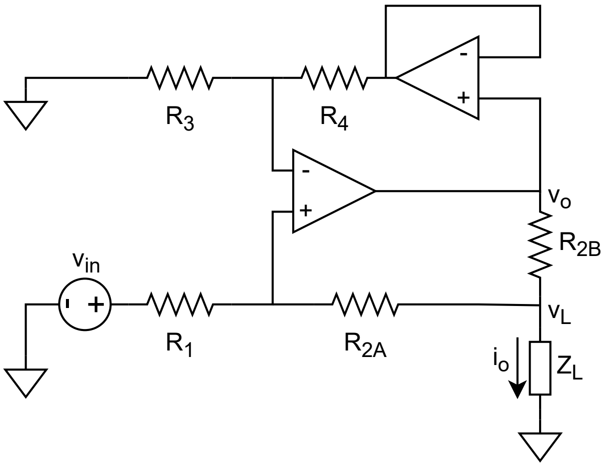

Figure 3.11: Improved Howland Current Source with buffer.

The first improvement is to divide the resistor R_2 into two resistors R_{2A} and R_{2B}, this change reduces the power losses caused by the resistor R_1 [41]. Due to this change, the balanced-bridge condition is now given by Equation 3.18.

$$\frac{R_{2A} + R_{2B}}{R_1} = \frac{R_4}{R_3} \tag{3.18}$$

With this improvement, the new transfer characteristic equation is given by Equation 3.19, keeping in mind that R_2 is the sum of the two resistors R_{2A} and R_{2B}.

$$i_o = \frac{R_2/R_1}{R_{2B}} v_{in} \tag{3.19}$$

The final improvement is the addition of a voltage follower circuit, also known as a buffer, in either the negative or the positive feedback path. This change allows for a higher output impedance seen by the load [42].

Furthermore, since this circuit uses a negative and a positive feedback path, this circuit may become unstable in certain conditions. However, the negative feedback path should always take over if the load is not an open circuit. One way to force this is to add parallel capacitors to R_1 and R_4, in the order of 10 pF [41]. Since this changes the frequency response of the current source, it was not implemented.

3.3.3 Effect of OpAmp Non-Idealities

While the analysis done previously used ideal OpAmps, using real OpAmps will yield different results. Real OpAmps have different parameters that must be taken into consideration while choosing which OpAmp to use.

Parameters like the Open Loop Gain, or Aol for short, reduce the maximum output impedance the OpAmp can reach [41, 42]. The Gain-Bandwidth Product (GBW), on the other hand, reduces the frequency band at which the output impedance remains constant. The GBW is a constant parameter from the OpAmp that indicates the maximum frequency it can operate at a unitary gain. That means that if an amplifier with GBW of 10 MHz operates with a gain of 10 kV/V, then the -3 dB point will be located at 1 kHz. As such, having a high Aol not only increases the output impedance but also decreases the maximum working frequency if GBW is not high enough.

The resistance between the differential ports, r_d, while ideally is infinite, in reality, it is typically in the order of 1 to 10 MΩ. Moreover, the OpAmp's internal output resistance, r_o, ideally 0 Ω, is usually close to 100 Ω. All these factors contribute to reducing the maximum output impedance achieved by the VCCS.

To demonstrate the effects of the Open Loop Gain and the GBW, the circuit in Figure 3.11 was simulated, in LTSpice [43], with the ideal model of an OpAmp. This model allows to change the Open Loop Gain and the GBW parameters individually and observe the changes in the results. Table 3.2 contains the parameters used for each OpAmp.

Table 3.2: Parameters used for the simulation.

	Aol [dB]	**GBW [MHz]**
OpAmp 1	80	10
OpAmp 2	110	10
OpAmp 3	110	1000

With these parameters, a frequency sweep was done from 1 Hz to 1 MHz to determine the output impedance of each amplifier, the results obtained are represented in Figure 3.12.

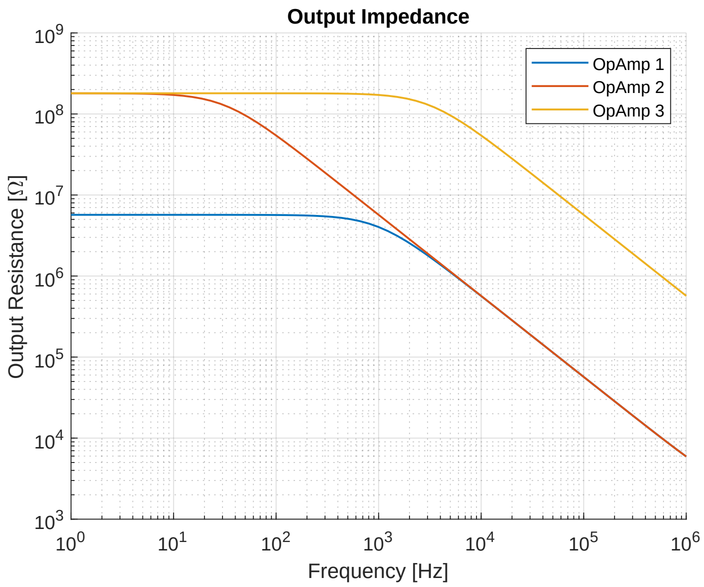

Figure 3.12: Output impedance versus amplifier parameters.

As previously stated, a lower Open Loop Gain yields a lower maximum output impedance, and this is possible to observe by comparing OpAmp 1 and OpAmp 2. By increasing the Open Loop Gain but maintaining the same GBW, the frequency band in which the output impedance remains constant decreases. Nonetheless, for higher frequencies, the output impedance converges to the same value. Finally, increasing the GBW doesn't affect the maximum output impedance but instead increases the region in which it remains constant.

3.3.4 Design and Simulation Results

Given the theoretical explanation of the VCCS, an Improved Howland Current Source was designed with a transconductance of 1.667 mA/V; this way, with an AC input signal of 0.3 V, the VCCS outputs an AC current of 500 µA. This value was chosen since it is lower than the recommended safety limit and to avoid saturating amplifiers in the presence of large impedances.

The OpAmps used for this circuit was the LMH6624 from Texas Instruments [44], which presents an Open Loop Gain of 81 dB with a GBW of 1.5 GHz. Table 3.3 contains the resistor values used for this circuit. Precision resistors with an accuracy of 0.1 % were used to avoid decreasing the output impedance due to resistor mismatches.

Table 3.3: Voltage Controlled Current Source Resistor Values.

R1	**R2a**	**R2b**	**R3**	**R4**
9 kΩ	28 kΩ	2 kΩ	9 kΩ	30 kΩ

By using LTSpice and the LMH6624 SPICE model provided by Texas Instruments, the designed VCCS was simulated with an input signal of 0.3 V at a frequency of 100 kHz for a load ranging from 10 Ω to 10 kΩ. The resulting output current is presented in Figure 3.13.

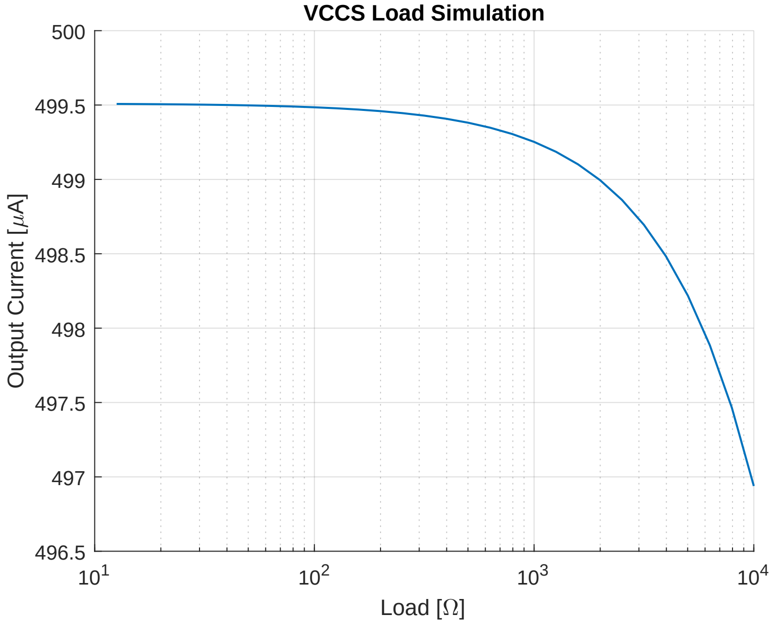

Figure 3.13: Output current of the designed VCCS for different loads.

From Figure 3.13, it is possible to observe that the output current greatly decreases with the increase of the load. One way to avoid this is to use an amplifier with better characteristics, such as the AD8099 from Analog Devices [45]; however, due to the silicon shortage and other current events, this amplifier isn't available for sale.

An issue, not presented in the previous graph, is the maximum output load. Due to the nature of the AC simulation, the OpAmps output swing is not simulated. For this specific amplifier, the maximum output load is 5 kΩ using a supply of ± 5 V. To drive bigger loads, it is necessary to increase the power supply's voltage.

The VCCS output impedance is calculated by first changing the load to a high value which, in this case, the value used was 1 GΩ. Afterwards, the formula for the current divider is used to calculate the impedance seen from the load since the theoretical current is known. Figure 3.14 presents the calculated output impedance.

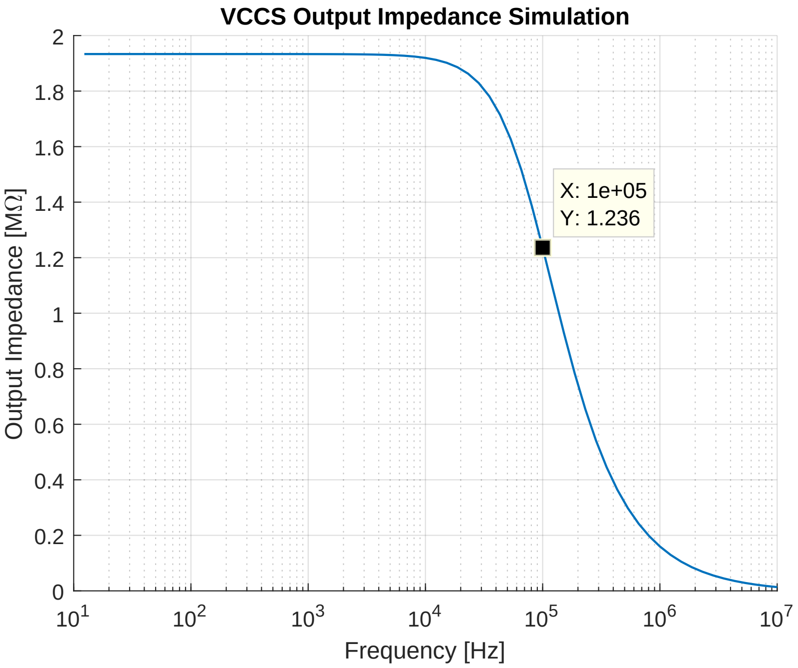

Figure 3.14: Output impedance of the designed VCCS.

As it is possible to observe, the output impedance is about 1.9 MΩ until the 10 kHz mark, at which it starts to drop significantly. Nonetheless, at the maximum operating frequency of the system, the output impedance is still above 1.2 MΩ.

3.3.5 Designed VCCS evaluation

A variable load resistor in series with a 10 Ω shunt resistor and an 8-bit oscilloscope was used to measure the VCCS performance. Channel one was connected to the VCCS input, and channel two to the shunt resistor. The Root Mean Square (RMS) value from both channels was registered in an Excel spreadsheet, and the output current was calculated. Measuring both channels allows for any errors from the signal generator to be compensated in the calculations. All resistors were measured beforehand with a multimeter and their real values taken into account.

In Table 3.4, the current is presented as a function of the frequency and load. It is necessary to keep in mind that these measurements include the band-pass filter, which will increase the measured error.

Table 3.4: Designed VCCS current, in µA, versus output load and frequency.

	1 kHz	**2 kHz**	**5 kHz**	**10 kHz**	**20 kHz**	**50 kHz**	**100 kHz**
1 kΩ	490.2	494.3	497.0	501.2	506.6	503.9	509.4
2 kΩ	491.5	494.3	498.4	502.5	503.9	508.0	510.8
3 kΩ	491.5	494.3	497.0	502.5	501.2	508.0	510.8
4 kΩ	491.5	495.7	503.9	503.9	503.9	508.0	512.1
5 kΩ	494.3	495.7	503.9	503.9	503.9	509.4	514.9

In the previous table, it is possible to observe a tiny variation in the flowing current for the same frequency, which is expected since the output current should be load-independent. Higher output loads cause a deformation of the output current waveform due to the OpAmp's limitations, which cause the oscilloscope to present a wrong RMS value, explaining the variations.

A higher variation is observed for the same output load but different frequencies, which is not expected since the simulation indicates that only after 100 kHz the output impedance drops significantly. There are many reasons for this occurrence; however, the most probable is the usage of a breadboard and long wires, which create unwanted parasitics. One other possible cause for this issue is the use of the designed signal generator board for the input signal, which, although it presents fairly good frequency accuracy, also presents faint amplitude variations.

3.4 Multiplexing System

Since this project employs a single-source architecture with 32 electrodes, it is necessary to include a multiplexing system to alternate between all possible electrodes. For systems with 32 or fewer electrodes, a simple analog multiplexer IC does the job; however, for systems that use more than 32 electrodes, it is necessary to use a Crosspoint Switch (CPS) to alternate between electrodes.

The multiplexer IC approach works well for systems with 16 electrodes since there is a variety of commercially available multiplexer ICs with different properties; however, for 32 electrodes, only one IC was found, the AD732 from Analog Devices [**?**].

Although the mentioned IC has 32 analog channels and a low on-resistance of about 4 Ω, its maximum power supply range is ±2.5 V, which, coupled with a fixed current value, limits the maximum load for the VCCS. For a simple system that uses two electrodes to inject current and other two to measure a voltage, a total of four AD732 ICs are necessary.

3.4.1 Multiplexing board on-resistance measurement

A multimeter was used to measure the designed multiplexing board on-resistance, the resistance between the analog input and the different analog outputs for all the AD732 present on the board. In Table 3.5 the measured on-resistance values are presented.

Table 3.5: Multiplexing board on-resistance measurement, in Ω.

	1	**2**	**3**	**4**	**5**	**6**	**7**	**8**	**9**	**10**	**11**	**12**	**13**	**14**	**15**	**16**	**17**	**18**	**19**	**20**	**21**	**22**	**23**	**24**	**25**	**26**	**27**	**28**	**29**	**30**	**31**	**32**
M1	3.9	4.1	4.1	3.9	3.9	4	4	4.1	3.8	3.9	3.9	4	3.8	4	3.8	3.9	4	4.1	4.1	3.9	4	4	4.1	4	3.9	3.9	3.9	4	3.9	4	4	3.9
M2	3.8	4	4	3.7	3.8	3.9	4	4	3.8	3.8	3.9	4	3.8	4	3.8	3.8	3.9	4	4.1	3.9	3.9	4	4.1	4	3.8	3.8	3.8	3.9	3.8	3.9	3.9	3.9
M3	3.7	4	4	3.7	3.8	3.9	3.9	3.9	3.7	3.8	3.8	3.9	3.7	3.9	3.9	3.8	3.8	3.9	4	3.7	3.8	3.9	3.9	4	3.7	3.7	3.7	4.1	3.7	3.8	3.8	3.7
M4	3.7	3.9	3.8	3.7	3.8	3.8	3.9	3.9	3.7	3.7	3.7	3.8	3.7	3.9	3.8	3.8	3.8	3.9	3.9	3.7	3.8	3.8	3.9	3.9	3.8	3.7	3.7	3.8	3.7	3.8	3.9	3.8

As it is possible to observe in the previous table, the minimum and maximum on-resistance measured were 3.7 Ω and 4.1 Ω, respectively, with an average on-resistance of 3.87 Ω and the standard deviation of 0.11 Ω. Overall, the results obtained are better than the 4 Ω on-resistance advertised in the datasheet. Since no multiplexer presented a difference between channels greater than 0.4 Ω, the on-resistance flatness was better than the advertised 0.5 Ω.

3.5 Programmable Gain Amplifier

There are two ways of measuring the voltage of the electrodes. In a single-ended system, the voltage is measured between an electrode and the ground potential, while in a differential system, the voltage is measured between two different electrodes.

Both systems present advantages and disadvantages. An advantage of differential measuring systems is that the dynamic range of the measured signal is lower due to the proximity of the electrodes, reducing the ADC's requirements over single-ended measuring systems. However, due to the nonzero common-mode gain, A_{CM}, the error in these systems increases when compared to single-ended measuring systems since these measurements do not present a common-mode [46].

3.5.1 Differential and Common-Mode signals

Given an instrumentation amplifier, a type of differential amplifier with high input impedance, with differential and common-mode gains of A_D and A_{CM}, respectively, and input signals V^- and V^+, then the output signal resulting is given by Equation 3.20,

$$V_o = A_D V_D + A_{CM} V_{CM} \tag{3.20}$$

Where V_D is the differential portion of the input signals given by $V_D = V^+ - V^-$ and V_{CM} is the common-mode portion given by $V_{CM} = (V^+ + V^-)/2$.

In an ideal instrumentation amplifier, the common-mode gain is zero, making the output signal just the differential portion of the input signals. However, due to small mismatches in the input impedances of the different amplifier's inputs, a small leakage is bound to happen, which makes the common-mode gain nonzero [46].

A parameter referred to when using these amplifiers is the CMRR, which represents the ratio between the amplifier's differential gain and the amplifier's common-mode gain, as presented in Equation 3.21.

$$CMRR = 20 \log_{10} \left(\frac{A_D}{A_{CM}} \right) \tag{3.21}$$

Usually, the CMRR is a positive value; however, when given as a negative value, it means that the fraction inside the logarithmic portion is inverted.

3.5.2 Design and Simulation Results

For this module, an AD8253 IC from Analog Devices [47] was chosen. This IC is recommended for biomedical applications, presents four gain steps of 1, 10, 100 and 1000 V/V, a large GBW parameter and a CMRR of 100 dB from DC to 20 kHz and above 60 dB at 100 kHz. This IC also presents an output offset pin, which makes it easier to use with an ADC. All these characteristics, combined with only three pins to set and latch the gains, make it a good choice for this system. Many other PGAs in the market usually present high gains but with lower GBW, making it unusable in higher frequencies.

Since the IC output swings roughly ±1.3 V from the supply voltage, a differential supply of ±5 V is used with an output offset of 2 V. As the input signal comes from the electrodes, the filter designed in Section 3.2 was placed at the IC's input.

Figure 3.15 presents the simulated transfer function for the AD8253, where the solid lines refer to the left most Y axis and the dashed lines refer to the right most Y axis.

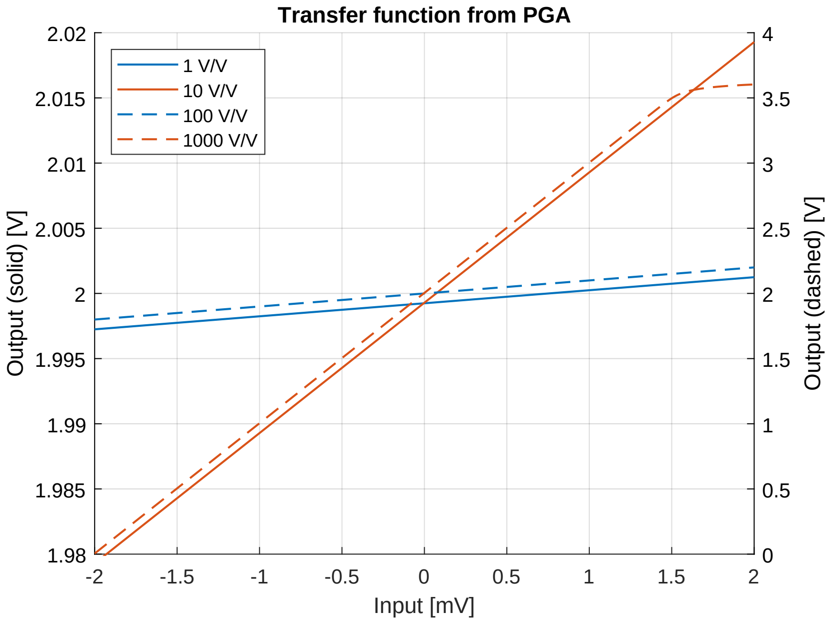

Figure 3.15: AD8253 simulated transfer function.

Although it is hard to observe, the simulations present that the IC works as pretended and that the maximum output voltage is about 3.6 V. Given that the output voltage is about 2 V for an input voltage of 0 mV for all gains, it is possible to verify that the output offset reference works as intended.

3.6 Analog-to-Digital Converter

After the signal from the electrodes has been filtered and amplified, it is ready to be read by the microcontroller. As such, an Analog-To-Digital Converter (ADC) is needed for this task.

An ADC is a type of IC that receives an analog voltage, typically between 0 V and V_{REF}, and ties it to a binary word with its length defined by the ADC bit resolution. The ADC IC can be described by the following characteristics:

- Resolution, in bits;
- Maximum sampling frequency, in Samples per Second (SPS);
- Number of input channels;
- Architecture;
- Input Type.

For this project, given the importance of the read value's accuracy, a minimum resolution of 12 bits was decided, which, for a reference voltage of 3.6 V, yields a Least Significant Bit (LSB) value of about 879 µV. Higher bit resolution would improve the system but make driving the ADCs much harder and, if proper care is not taken, could harm the system's performance. By using Equation 3.22 [48], where N is the number of bits, one can calculate that the quantization SNR of a 12-bit ADC as roughly 74 dB.

$$SQNR_{dB} = 6.02N + 1.76 \tag{3.22}$$

A minimum sampling frequency of 200 kSPS is needed to comply with Nyquist's Theorem due to the maximum work frequency of 100 kHz; however, to also avoid sampling the signal with a low temporal resolution, it was decided to use a sampling frequency of 1 MSPS.

It is important to note that there are methods to allow using a maximum sampling frequency below the maximum work frequency due to the repeating nature of a sinusoidal wave; however, to decrease the system's complexity, these methods will not be used.

3.6.1 Peak Detector

To allow faster measurements and decrease ADC's sampling frequency requirements, a peak detector was added to the module board. The peak detector included has a few improvements over the typical diode-capacitor one. The implemented peak detector circuit is shown in Figure 3.16.

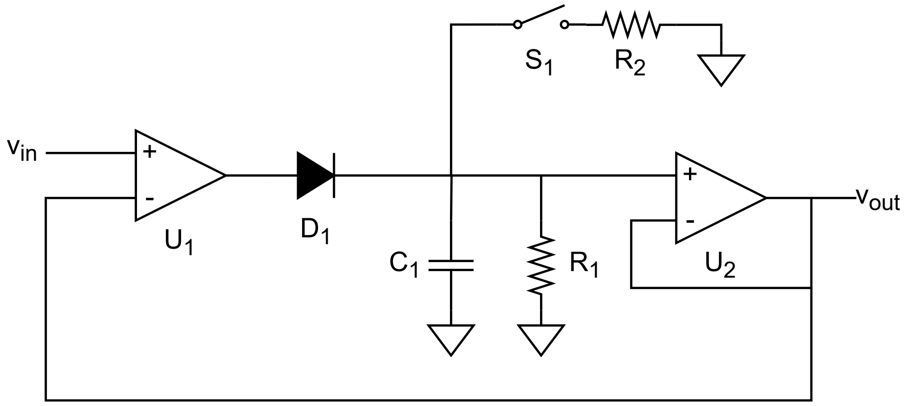

Figure 3.16: Implemented high-speed peak detector's schematic.

In this circuit, U_1 is a comparator while U_2 is a normal OpAmp. A comparator is a special type of OpAmp used only to compare two input voltages, which allows for high-speed switching between its off and on states.

Ignoring the switch S_1 and resistor R_2, this circuit only has two states: whenever V_{out} is greater than V_{in}, the comparator is off, which means that its output is at 0 V, reverse biasing the diode D_1 and discharging the capacitor with a time constant, τ, equal to R_1C_1. Whenever V_{in} is greater than V_{out}, the comparator is on, outputting V_{CC}, directly biasing diode D_1 and charging the capacitor C_1 until its voltage is greater than V_{in}, entering the first state described.

By introducing the switch S_1 and resistor R_2, it is possible to dynamically reset the capacitor's voltage with a microcontroller by changing the time constant to $\tau = (R_1||R_2)C_1$; however, if $R_2 \ll R_1$ then $\tau \approx R_2C_1$, ignoring any parasitics introduced by the switch.

The component values used in this module are presented in Table 3.6.

Table 3.6: Peak detector component values.

	U1	U2	S1	D1	R1	R2	C1
Value	LTC1719	LT1818	ADG701	1N4148	2 MΩ	100 Ω	20 nF

3.6.2 Anti-Aliasing and Charge-Bucket Filter

While using an ADC, it is recommended to include a low-pass filter at its inputs to remove any aliasing caused by high-frequency noise that ends up being interpreted as a lower frequency. Following any ADC datasheet, a simple single-pole RC filter is indicated, as shown in Figure 3.17, also called a charge-bucket filter.

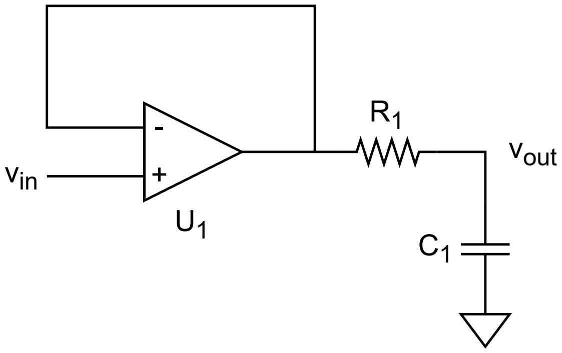

Figure 3.17: ADC’s charge-bucket filter.

For this type of filter, the cut-off frequency is given by Equation 3.23, which, with the recommended resistor of 50 Ω and capacitor of 47 pF from the ADCs datasheet [49], gives a cut-off frequency of 67 MHz.

$$f = \frac{1}{2\pi R_1 C_1} \tag{3.23}$$

This filter also works to avoid any capacitor charge kickback that happens whenever the ADC enters sampling mode. The capacitor charge kickback is caused by the sampling capacitor inside the ADC and, if not accounted for, can severely distort the input signal [50, 51].

For this module, the LTC2365 from Analog Devices [49] was used, which is a 1 MSPS, 12-bit, single-ended ADC with an external reference voltage pin, in this case, 3.6 V generated by a voltage regulator.

Unlike many ADC ICs, the conversion process is fully compatible with the SPI interface, which allows the full 12-bit resolution and the maximum sampling rate of 1 MSPS to be used with an SPI clock of 16 MHz.

4

Software implementation

In this Chapter, a brief description of the system's digital section is given. Since this document topic is more hardware-related, this Chapter will only mention the measurement software flowchart, the SPI Protocol and the problems detected while using it on the Raspberry Pi. Finally, a theoretical explanation of the I/Q Demodulation is given since this was the chosen approach to process the sampled analog signal read from the ADC, along with its advantages and disadvantages.

4.1 Software Flowchart

Given the flexibility in adding more digital processing blocks to the developed software, Figure 4.1 presents an example of the software currently implemented.

For example, right after obtaining the data from the ADC, a band-pass filter could be implemented along with another digital processing technique, such as an RMS calculation, to get the wave's amplitude.

So that in Figure 4.1 the value 160 mV doesn't appear as a random value, this was calculated using the ADC's voltage reference, 3.6 V, minus the PGA's voltage reference, 2 V, divided by the PGA's gain step of 10.

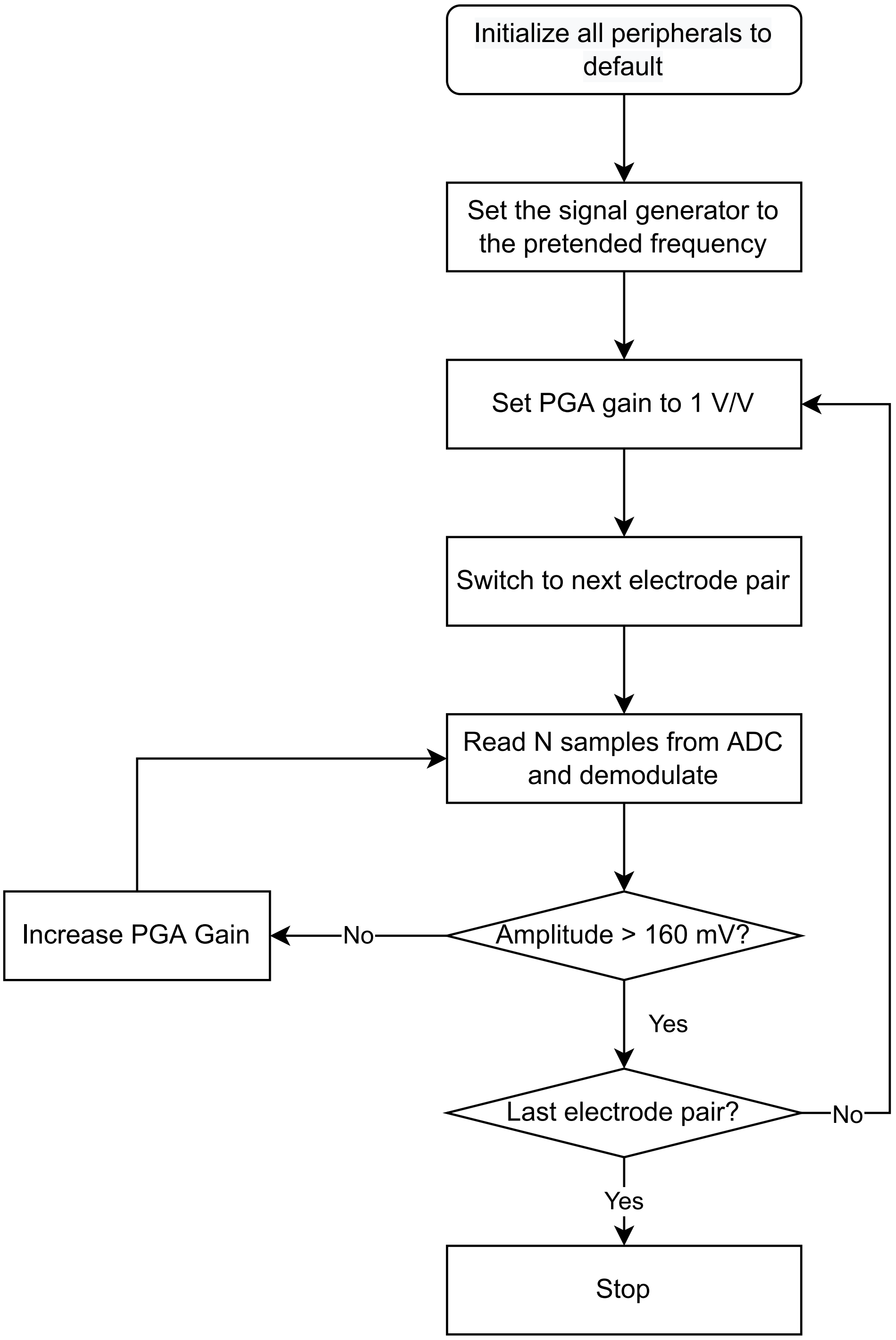

Figure 4.1: Flowchart of the Proposed Software.

One possibility for improvement is to choose a demodulation technique based on the SNR of the acquired signal. If the signal's SNR is above a certain threshold, no further filtering is needed and, as such, computational power is saved.

4.2 SPI Protocol

The SPI protocol is a protocol commonly used in high-speed (less than 10 MSPS) ADCs. This type of protocol follows the Master-Slave-based architecture in which one device assumes the role of Master, typically the microcontroller, and the Slaves are only allowed to talk when selected [52].

This type of architecture allows multiple Slaves to be present in the same bus without interference, as long as proper signal routing is followed. It typically presents four signals: Master Out Slave In (MOSI), Master In Slave Out (MISO), Serial Clock (SCLK) and Chip Select (CS); however, the first two can be terminated if not used, for example, in devices that don't report anything to the Master (as long as there are no other devices on the bus).

4.2.1 SPI Data Transfer and Modes

The SPI data transfer begins when the Master pulls the CS line of a Slave low since these lines are usually active low and, after a delay in the order of nanoseconds, it pulses the SCLK line with a fixed frequency. The SCLK line is used to indicate when to sample and when to shift the contents to the device's internal buffers.

The protocol presents two major parameters: the Clock Polarity (CPOL) and the Clock Phase (CPHA). Table 4.1 presents the four possible combinations of the parameters, as well as their differences.

Table 4.1: SPI Modes (adapted from [52]).

SPI Mode	CPOL	CPHA	Clock Polarity in Idle	Clock Phased used to Sample
0	0	0	Logic Low	Data sampled on rising edge
1	0	1	Logic Low	Data sampled on falling edge
2	1	0	Logic High	Data sampled on rising edge
3	1	1	Logic High	Data sampled on falling edge

When using multiple Slaves in the same bus, care should be taken as some Slaves support multiple SPI modes, but some only support one. Given the physical difference of these modes, they are incompatible with each other. In this document, the SPI Mode 0 was used for the ADC and the SPI Mode 2 was used for the signal generator.

4.2.2 SPI Limitations on the Raspberry Pi

Currently, there are multiple C libraries that implement an Hardware Abstraction Layer (HAL) Application Programming Interface (API) for the SPI protocol, such as the BCM2835 [53]. Unfortunately, as with many HALs, an overhead is created to check that all parameters are according to the specifications. As such, every SPI action takes longer than it should, creating a slight mismatch between the expected sampling frequency and the real sampling frequency.

The biggest issue, however, is the use of the Linux operating system. Given the architecture of the Linux kernel, it is possible for the thread used for the SPI action to be interrupted or to suffer a context switch. In any case, a delay of hundreds of microseconds occurs, completely degrading the pretended sampling frequency.

There are many possible solutions to this problem; however, the less complex is to redo the sampling if a delay higher than acceptable is detected. While a wasteful solution, it is one solution that is ensured to work with every Linux kernel version.

4.3 I/Q Demodulation

I/Q demodulation, is a form of demodulation typically used in High-Frequency (HF) systems to obtain information about the amplitude and phase of the input signal with respect to the system's local oscillator (LO) [54].

This type of demodulation is commonly used in homodyne and heterodyne receiver systems since it removes the need to sample the entire signal to obtain the information. In Figure 4.2, a block diagram of an I/Q demodulator is presented.

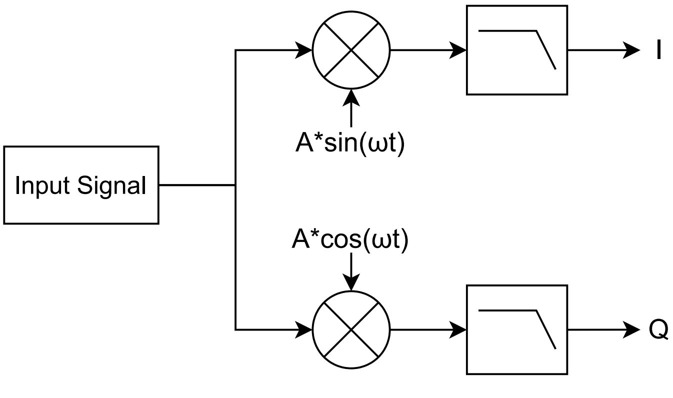

Figure 4.2: I/Q Demodulator Block Diagram.

4.3.1 Principle of operation

The I/Q demodulator works by multiplying the input signal with a sinusoidal wave, which results in the input signal's frequency shifting to both the sum and the subtraction between the input signal's frequency and the local oscillator frequency. For the upper path of the signal, the result is given by the following result [54]:

$$I(t) = A_{in} \sin\left(2\pi f_{in} t + \phi_{in}\right) \times A_{LO} \sin\left(2\pi f_{LO} t\right) \Leftrightarrow$$

$$\Leftrightarrow I(t) = \frac{A_{in} A_{LO}}{2} \left(\cos\left(2\pi f_{in} t - 2\pi f_{LO} t - \phi_{in}\right) - \cos\left(2\pi f_{in} t + 2\pi f_{LO} t + \phi_{in}\right)\right)$$

By rearranging the previous equation, Equation 4.1 is obtained.

$$I(t) = \frac{A_{in} A_{LO}}{2} \left(\cos\left(2\pi (f_{in} - f_{LO}) t + \phi_{in}\right) - \cos\left(2\pi (f_{in} + f_{LO}) t + \phi_{in}\right)\right) \tag{4.1}$$

Following the same steps for the bottom path, the result is given by Equation 4.2.

$$Q(t) = \frac{A_{in} A_{LO}}{2} \left(\sin\left(2\pi (f_{in} + f_{LO}) t + \phi_{in}\right) + \sin\left(2\pi (f_{in} - f_{LO}) t + \phi_{in}\right)\right) \tag{4.2}$$

The usage of a subsequent filter is necessary to remove the signal created located at the sum of the two frequencies. One interesting result of the previous equations is what happens if the LO frequency is equal to the input frequency. After filtering, if the frequency of the LO is the same as the input frequency, each path will present a DC voltage given by Equations 4.3:

$$\begin{cases} \overline{I} = \frac{A_{in} A_{LO}}{2} \cos\left(\phi_{in}\right) \\ \overline{Q} = -\frac{A_{in} A_{LO}}{2} \sin\left(\phi_{in}\right) \end{cases} \tag{4.3}$$

Given the last equations, and forcing the LO to produce a signal with unitary amplitude, it is possible to calculate the amplitude of the input signal with Equation 4.4.

$$A_{in} = \sqrt{4\overline{I}^2 + 4\overline{Q}^2} \tag{4.4}$$

The phase of the input signal is given by Equation 4.5.

$$\phi_{in} = \arctan\left(\frac{\overline{Q}}{\overline{I}}\right) \tag{4.5}$$

4.3.2 Advantages and Disadvantages

Although this demodulation scheme seems pretty simple, it is very helpful in measuring the amplitude of signals with fairly low SNR. To prove this point, a simulation was done where an input signal of 1 V, with a frequency of 10 kHz, an arbitrary phase and an SNR varying from 0 to 90 dB was demodulated. Figure 4.3 presents the measured error, in percentage.

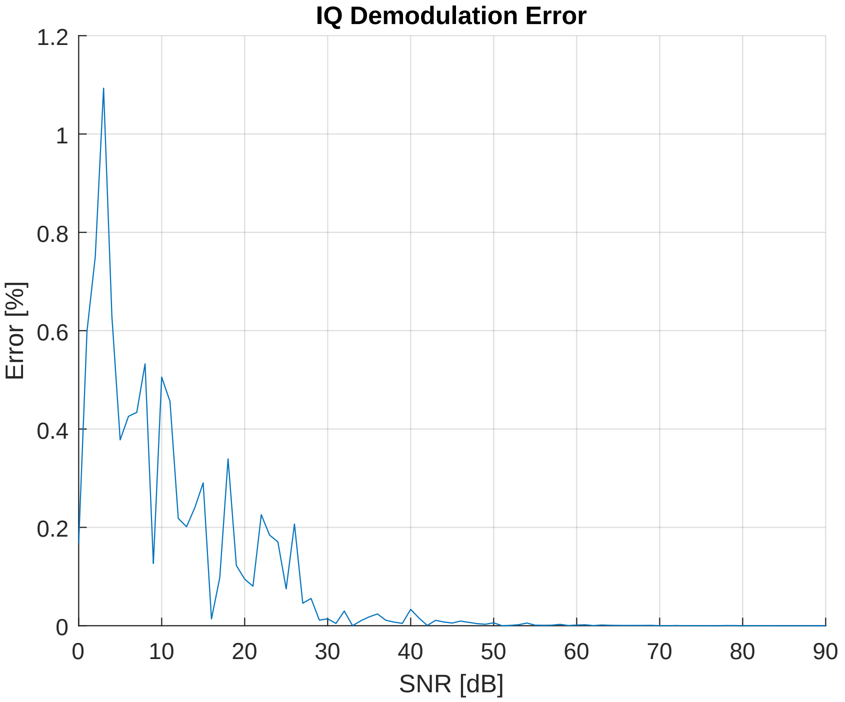

Figure 4.3: I/Q Demodulator Accuracy Error.

As it is possible to observe from Figure 4.3, the maximum measured error was just 1.1 % with an SNR of 3 dB, which is a fairly low SNR. At 27 dB, the error drops below 0.04 %, which is equivalent to an error of 400 µV. At 42 dB, the error is only 50 µV.

It must be brought to attention that the values shown on the graph are not exact. Since the added noise is gaussian, different iterations of the simulation will yield different noise values, thus different errors. In Figure 4.4, the demodulation plot is shown, as well as the reference input signal.

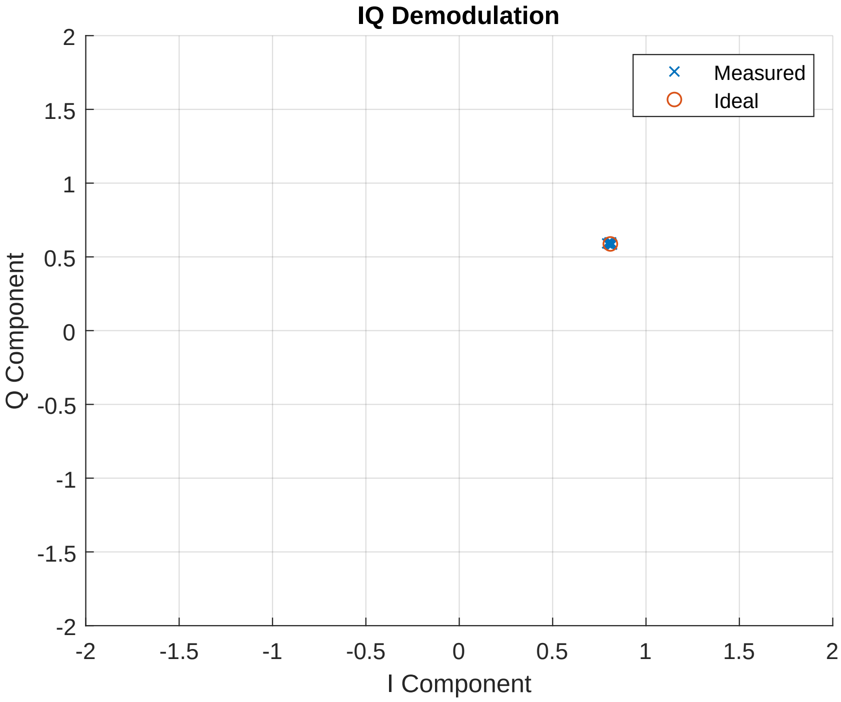

Figure 4.4: I/Q Demodulator Plot.

One other advantage of this demodulation scheme is the possibility of fitting the input signal (to a certain degree of accuracy) to a perfect sine wave, with the amplitude given by Equation 4.4 and the phase by Equation 4.5, and using this signal to calculate an approximate SNR value.

First, it is necessary to calculate the RMS value from the ADC measured values, RMS_{ADC}. This is done by using Equation 4.6, which is the generalized equation for the RMS value of a discrete function with n points.

$$RMS = \sqrt{\sum_{i=1}^{n} \frac{x_i^2}{n}} \tag{4.6}$$

Afterwards, it is necessary to calculate the RMS noise, RMS_{noise}, which is done by calculating the RMS value of the subtraction between the ADC values and the reconstructed signal. Inputting the calculated RMS values in Equation 4.7, gives the approximate SNR, in dB.

$$SNR = 20 \log \left(\frac{RMS_{ADC}}{RMS_{noise}} \right) \tag{4.7}$$

Although this scheme presents a few advantages, the major disadvantage is its computational cost. Even if the oscillator is implemented using lookup tables to remove the cost of calculating the same sine and cosine coefficients every time, floating-point calculations can be expensive in low-power microcontrollers, increasing the time between frames.

5

System Results and Discussion

In this Chapter, the results obtained from the complete prototype are presented. These results range from simple experiments to evaluate the system's performance to more complex EIT scenarios, such as imaging of a human arm or a breast phantom. Afterwards, the previous prototype, presented in Section 1.2, and the developed prototype are compared.

5.1 Result Discussion

This Section presents the results and the conclusions drawn with an overall of three tests effectuated. The first test, the resistor breakout, was developed to understand the accuracy and precision of the system in measuring the voltages for each pair of electrodes. The second test, the human arm test, was done to observe the system's response to AgCl electrodes and a more realistic scenario. Afterwards, a breast phantom test set was used to test the system in its original usage scenario. Finally, a water tank was developed to evaluate the system's performance in a dynamic scenario.

5.1.1 Resistor Breakout

This test consists in measuring a total of 9 resistors to evaluate the measured values and their variability between measurements. For this purpose, a breakout board was created with the following 10 % tolerance resistors connected in series: 1x 1 kΩ, 2x 820 Ω, 2x 270 Ω, 2x 180 Ω and 2x 10 Ω, as depicted in Figure 5.1.

Figure 5.1: Developed Resistor Breakout Board.

These resistor values were chosen to force the system to use different PGA gains during the measurements without saturating the system itself since the total resistance is 3.56 kΩ. In Table 5.1, the real resistor values are presented, measured with a multimeter.

Table 5.1: Expected and Measured Resistor Values, in Ω.

	R1	**R2**	**R3**	**R4**	**R5**	**R6**	**R7**	**R8**	**R9**
Expected	1k0	820	820	270	270	180	180	10	10
Measured	985	810	810	266	265	176	177	10.4	10.4

The expected set gains are 1 V/V for the first three resistors, 10 V/V for the following four resistors and 100 V/V for the last two resistors. Due to a lack of lower-value resistors, the 1000 V/V gain setting remains untested.

This test is divided in three smaller tests, the total resistance measurement test, the differential resistance measurement test and the precision test.

Total Resistance Measurement

For this test, the current is injected in connector number 1 and sank in connector number 10. For the measurement part, one of the measuring connectors is fixed at number 10 while the other alternates between the different resistors (connectors 1 through 9). The test frequency used was 10 kHz for no reason other than to make the measurement faster.

Figure 5.2a presents the measured voltage at each connector and Figure 5.2b presents the error between the measured value and the simulated values, using the measured resistor values in Table 5.1. Since these measured values weren't made with a precise multimeter, a small error is expected. Although the maximum error is about 28 mV, or 1.62%, this error is the sum of all errors caused by the other resistors.

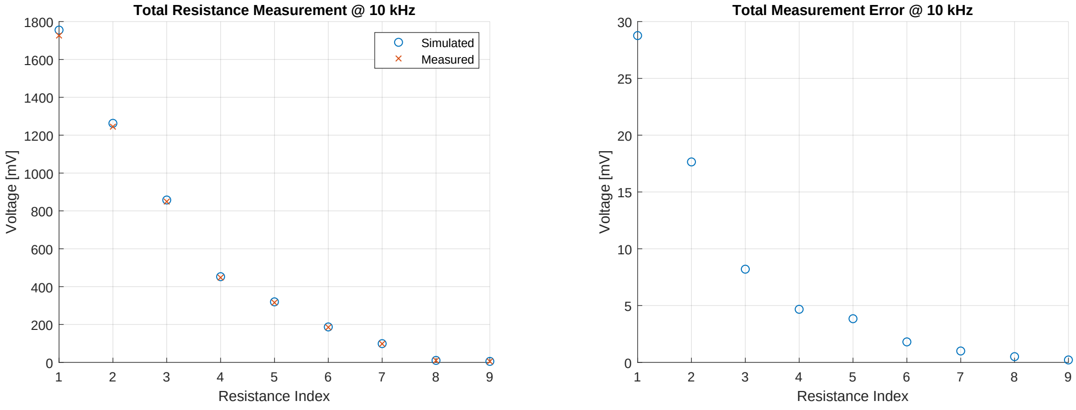

(a) (b)

Figure 5.2: Total Resistance Measurement: (a) Voltage, (b) Error.

Differential Resistance Measurement

As in the previous test, the current is injected between connectors 1 and 10. The measurement, however, is done between each resistor's connectors. This method has an advantage over the last since it reduces the measured error by not accounting for the other resistors, reducing the impact of the multimeter error.

In similar fashion to the last test, Figure 5.3a presents the measured voltage at each connector and Figure 5.3b presents the error between the measured value and the simulated values, using the measured resistor values in Table 5.1.

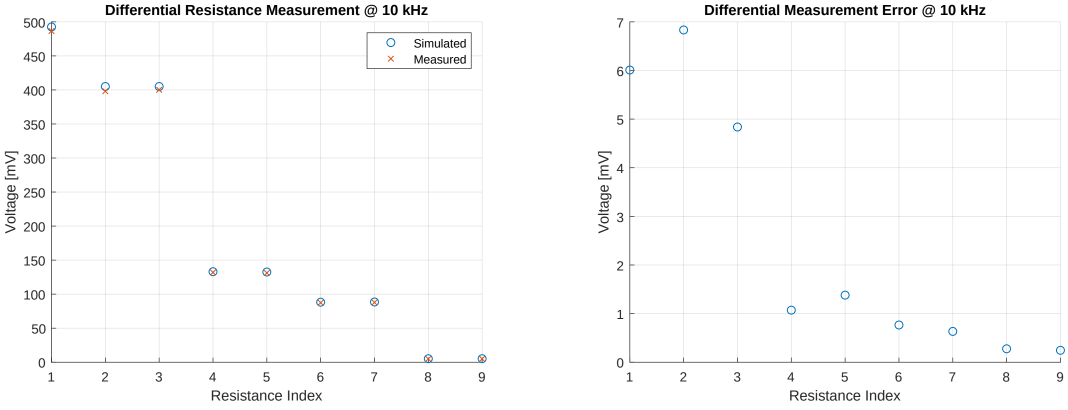

(a) (b)

Figure 5.3: Differential Resistance Measurement: (a) Voltage, (b) Error.

As it is possible to observe in the previous figures, and as expected given the results of the last test, the results obtained are pretty similar to the simulated ones; however, the new error values are lower, which given the previous explanation, is to be expected.

Notice that the first three resistors present a much larger error than the others, which is to be expected given the different PGA gain settings used since the first three resistors use a gain of 1 V/V, and the others use higher settings.

Higher PGA gains not only cause the ADC to perceive a much larger signal, which increases the SNR, but also causes the measurement error to be divided by the gain set, which only happens if the error is caused by the ADC itself.

Precision Test

Given the satisfactory results from the two previous tests, the differential test was executed 512 times consecutively, given this was the most realistic test, with the results saved to the computer. Figure 5.4 presents the results obtained.

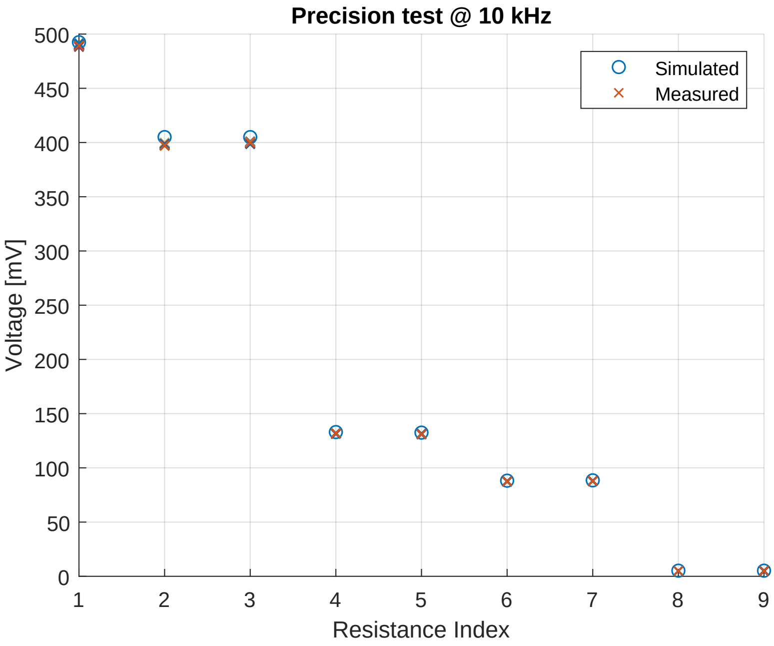

Figure 5.4: Differential Resistance Precision Test.

Given the proximity of the measured results in the presented graph, it is possible to observe that while the prototype has a slight offset, it shows a high degree of precision. A statistical analysis of the obtained results is given in Table 5.2.

As it is possible to observe in Table 5.2, the maximum standard deviation is 785 µV for the first resistor which, for the ADC full scale, is only a deviation of 0.024% and, as expected, this value decreases with the PGA's gain increase.

The absolute error presented is calculated using the measured mean values and the simulated values, resulting in a maximum absolute error of 4.3 mV for the third resistor, again, decreasing with the PGA's gain.

Table 5.2: Precision test expected and measured results, in mV.

		R1	**R2**	**R3**	**R4**	**R5**	**R6**	**R7**	**R8**	**R9**
Simulated		492.5	405	405	133	132.5	88.2	88.5	5.2	5.2
Measured	**Std**	0.785	0.378	0.391	0.0902	0.105	0.063	0.063	0.0048	0.005
	Min	486.8	399.8	398.6	131.4	130.7	87.4	87.7	4.91	4.93
	Mean	489.9	401.7	400.6	131.8	131.3	87.7	88	4.93	4.95
	Max	492	402.9	402.5	132.4	131.8	88.0	88.3	4.94	4.97
	Abs. Error	2.6	3.36	4.3	1.2	1.2	0.5	0.5	0.27	0.24
	Rel. Error	0.53%	0.83%	1.07%	0.89%	0.94%	0.57%	0.56%	1.5%	0.95%

5.1.2 Human Arm Test

In this test, four AgCl electrodes with an overall diameter of 5 cm were placed around a human arm. Using a measuring frequency of 10 kHz, an adjacent pattern and the D-Bar reconstruction algorithm [55], a medical image was produced and presented in Figure 5.5.

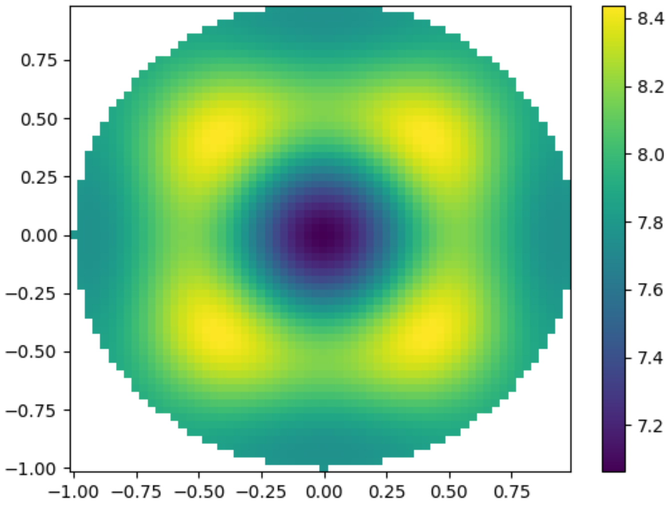

Figure 5.5: Reconstructed Human Arm.

In the Figure 5.5, the bar at the right of the image presents the conductivity in S/cm; however, given the inaccuracy of the reconstruction algorithm used, the numerical values should not be taken into consideration. In these images, the X and Y axis both represent a relative position and, as such, are adimensional.

To accurately analyze the medical image obtained, the structure of the arm is presented in Figure 5.6 in the form of a transversal cross-section. The yellow tissue represents fat, the red tissue represents muscle, and the white tissue represents the humerus bone, roughly at the center of the arm.

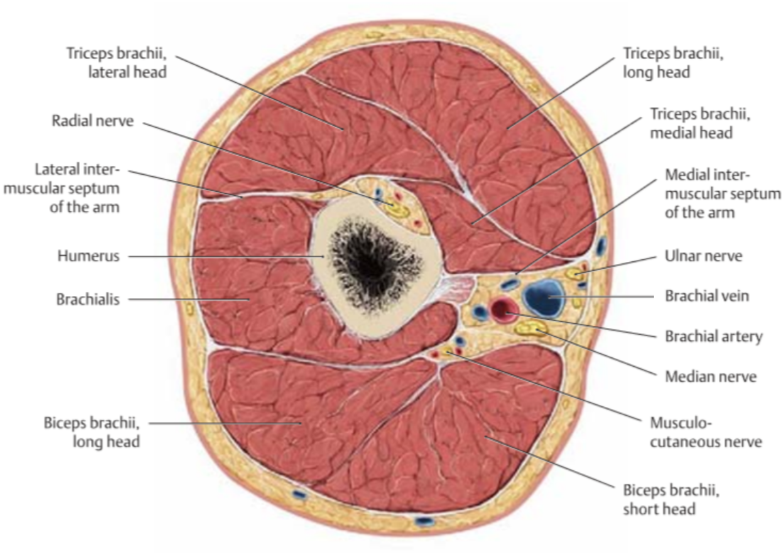

Figure 5.6: Human Arm Cross-Section (taken from [56]).

As it is possible to observe, the arm is composed of a thin layer of subcutaneous fat, that is, fat located beneath the skin which has a conductivity of 0.012 S/m, a thick layer of muscle which presents a conductivity of 0.202 S/m and the humerus bone with a center conductivity of 0.000975 S/m [57]. These conductivity values are for an unknown frequency; however, the ratio between them is what matters.

Referring back to Figure 5.5, it is possible to see a thin layer of medium conductivity tissue (fat), a thicker layer of higher conductivity tissue (muscle) and tissue in a cylindrical shape with the lowest conductivity (humerus bone).

5.1.3 Breast Phantom

For this test, a tumour phantom developed for Microwave Breast Imaging (MBI) applications was used. This phantom was developed using polyurethane rubber with graphite and carbon-black powders, for frequencies over 1 GHz [58]. While this phantom might give inaccurate conductivity values at lower frequencies, it should yield good medical images nonetheless.

The phantom is a homogeneous hemisphere with a diameter of roughly 136.7 mm with a hole of 25 mm to place a tumour plug to simulate and test different types of tissues with different electrical characteristics. This phantom was developed in [58] and is presented in Figure 5.7a and in Figure 5.7b. Both these figures present an upside-down view of the phantom, but in Figure 5.7b, the phantom has a tumour plug.

(a) (b)

Figure 5.7: Phantom Top View: (a) No plug; (b) Plug placed (taken from [58]).

The medical image in Figure 5.8 was produced using the previous prototype with an adjacent current injecting pattern in single-ended measurement, 12 electrodes, an unknown frequency and the D-Bar reconstruction algorithm.

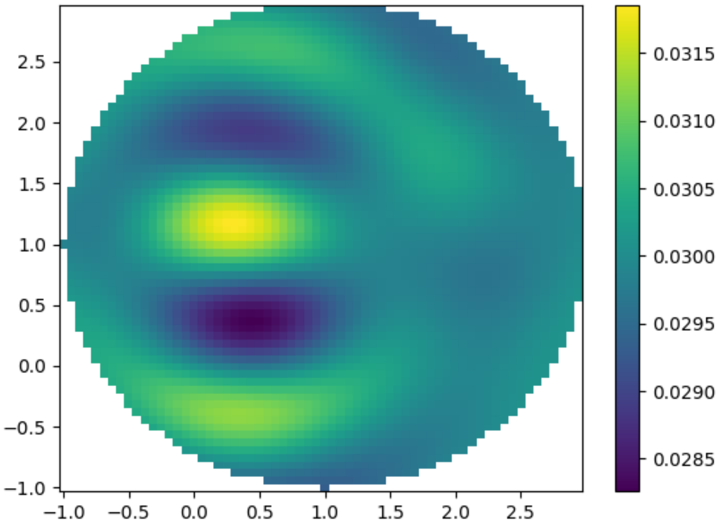

Figure 5.8: Phantom Medical Image Produced by the Previous Prototype.

As it is possible to observe in the previous figure, a somewhat round artifact with the highest conductivity is noticeable near to where the tumour plug is placed. The rest of the medium presents some variations over a complete homogeneous medium which is expected given the results obtained in [58].

Figures 5.9a and 5.9b were produced, for the frequencies of 1 kHz and 10 kHz, using the prototype developed in this document, eight electrodes, an adjacent current and voltage measuring pattern and the D-Bar reconstruction algorithm.

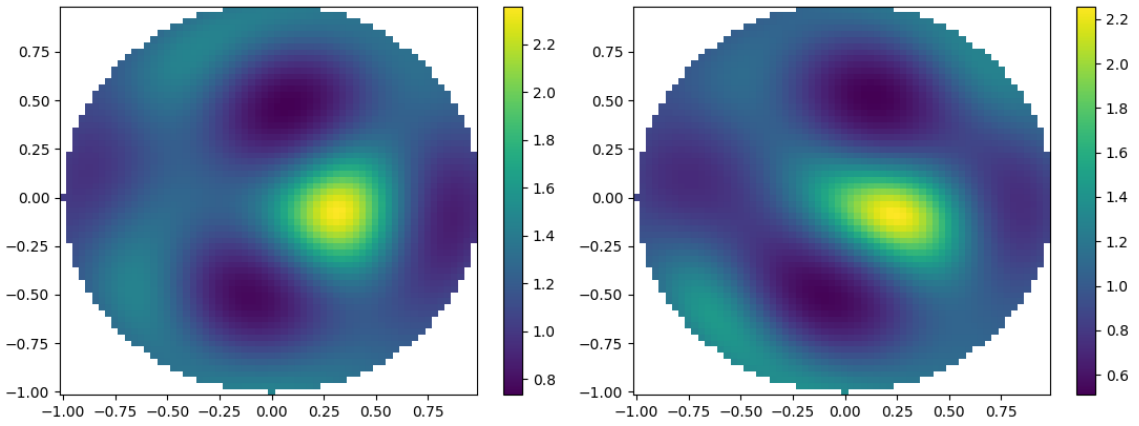

(a) (b)

Figure 5.9: Breast Phantom Imaging: (a) 1 kHz, (b) 10 kHz.

As it is possible to observe, both frequencies yielded a medical image similar to what is expected, given the phantom's composition. At 1 kHz, the tumour plug presents itself in a far more circular shape than at 10 kHz. The rest of the medium looks similar in both measuring frequencies, with two zones of lower conductivity surrounding the tumour plug, also observed in [58] (keeping in mind the lower image resolution produced by a lower frequency and number of electrodes).

Although the images produced by the developed prototype only used eight electrodes, which lowers the image resolution compared to 12 electrodes, the images produced by both prototypes are similar and are according to what is expected. Given the different number of electrodes and measuring frequencies, the images from both prototypes cannot be directly compared.

5.1.4 Water Tank

To further evaluate the developed prototype, a water tank was built and used. This water tank has an advantage over the last three tests since it is dynamic as it allows the introduction, removal or movement of the objects inside.

The water tank is composed of a cylindrical plastic recipient with a diameter of 11 cm and a height of 12 cm. To simulate the electrodes, 12 pieces of copper tape, with dimensions 1.27 cm by 12 cm, were placed around the recipient with wires soldered to avoid ripping the tape. The copper tape presents low resistance, and it is easy to replace. The inside view of the built water tank is present in Figure 5.10.

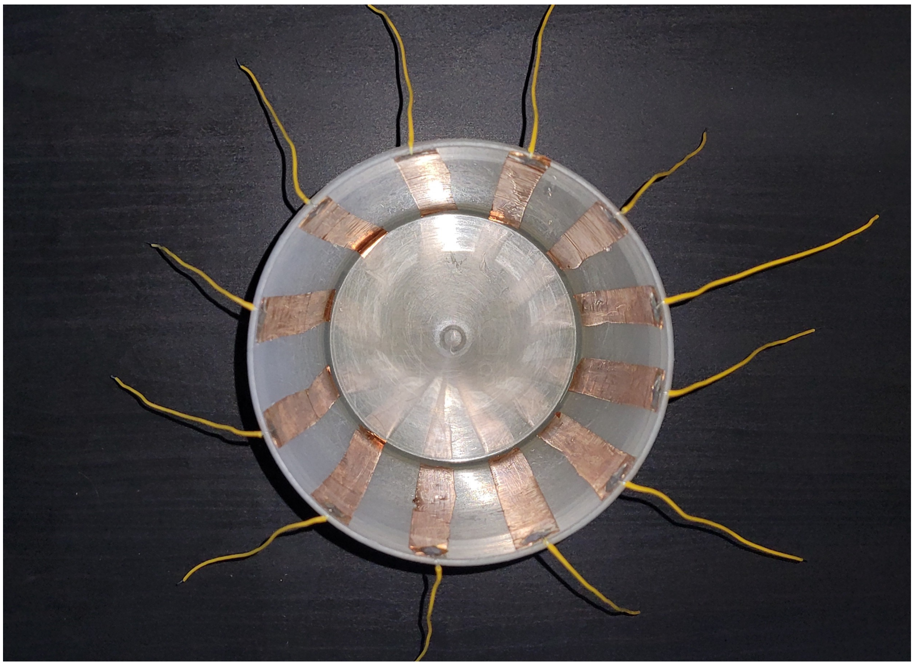

Figure 5.10: Water Tank Built for Testing.

In the previous figure, it is possible to observe that the copper tape pieces on the right side are grouped tighter than those on the left side, which might cause slight deformation on the final image.

For the following tests, two objects were used: a metal bullet, a highly conductive material, and a small glass cup, a good insulator. The following tests were realized with a 12-electrode adjacent current pattern and the time-difference D-Bar reconstruction algorithm, which uses a reference frame before any object is introduced and calculates the difference.

Bullet Test

Placing the metal bullet on the left side near the boundary and taking measurements at 1 kHz, yields the final image presented in Figure 5.11b with Figure 5.11a as a photographic reference.

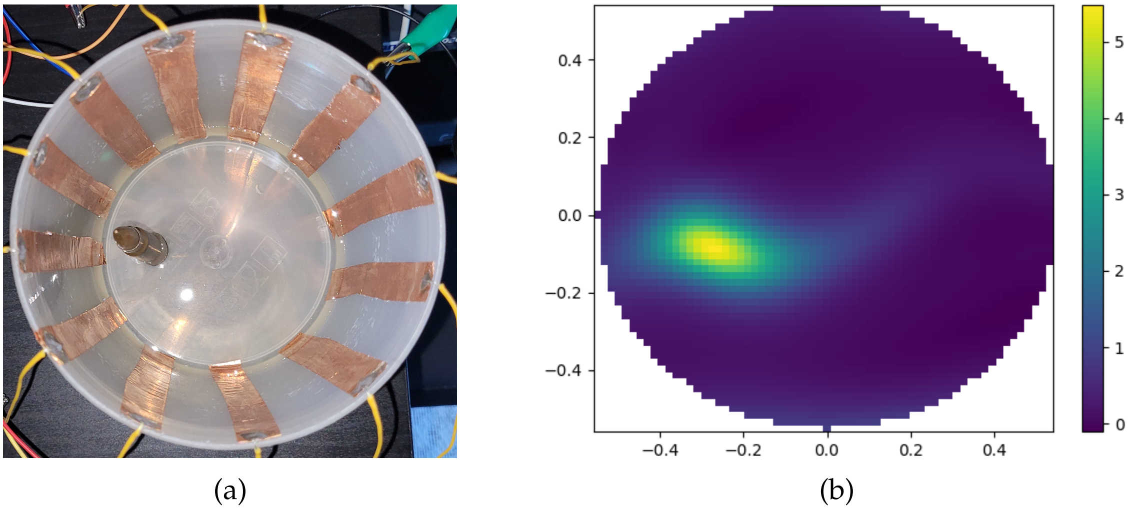

(a) (b)

Figure 5.11: Bullet Left Imaging: (a) Reference, (b) Reconstruction.

As it is possible to observe in the previous reconstruction, most of the image presents a null change in conductivity. The bullet's position, however, shows a positive number, meaning it detected an increase in conductivity (remembering that the D-Bar algorithm doesn't give accurate values), which is to be expected.

Repeating the measurement but moving the bullet slightly up, yields the image in Figure 5.12b with Figure 5.12a as a reference.

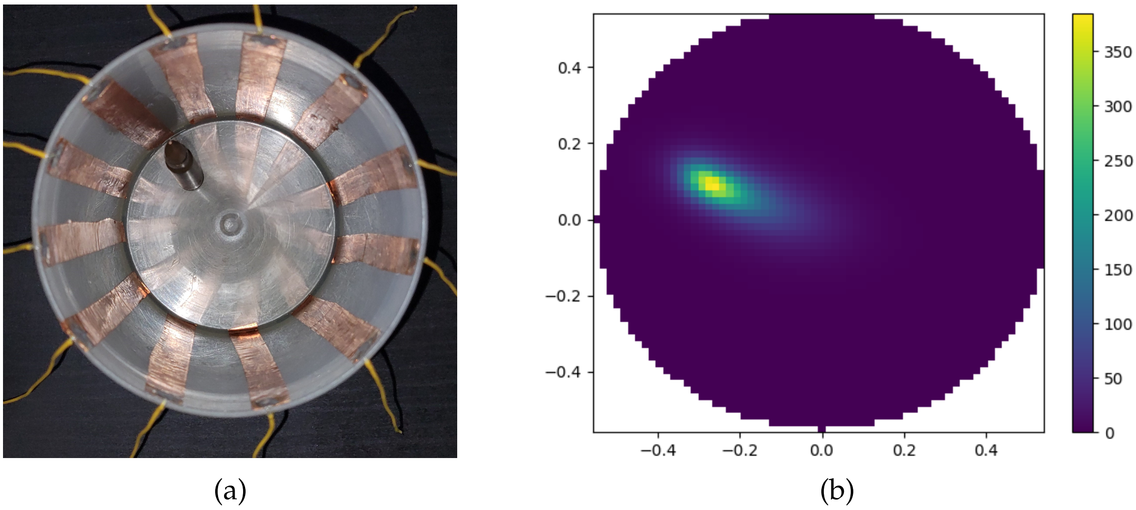

(a) (b)

Figure 5.12: Bullet Top-Left Imaging: (a) Reference, (b) Reconstruction.

Observing the previous two figures, it is possible to confirm that the bullet's new position is correctly identified, with a noticeable reduction of the artifact's size. Other than the unexpected reduction, the image is as expected.

Glass Cup Test

For this test, a small glass cup was placed inside the water tank near the left boundary, and some measurements were taken at 1 kHz and 10 kHz. Figure 5.13 presents a photographic reference of the water tank and in Figures 5.14a and 5.14b the reconstructed images measured at 1 kHz and 10 kHz, respectively. Note that the glass cup has a really low conductivity.

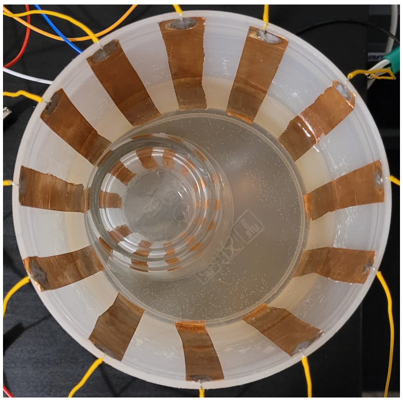

Figure 5.13: Glass Cup Left Imaging Reference.

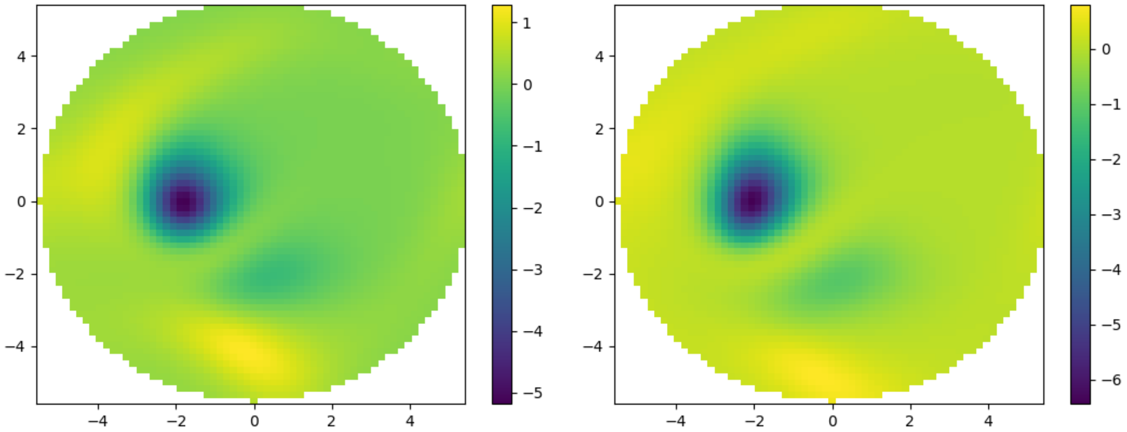

(a)

(b)

Figure 5.14: Glass Cup Left Imaging: (a) 1 kHz, (b) 10 kHz.

As it is possible to observe, the glass cup is correctly detected. It is also important to note that the detected conductivity is lower than that of the water, given that the detected value is negative.

By repeating the same test with the glass cup at the top, as indicated by Figure 5.15, the images in Figure 5.16a and 5.16b were obtained.

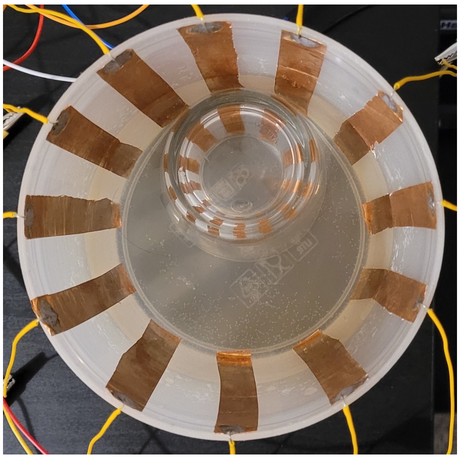

Figure 5.15: Glass Cup Top Imaging Reference.

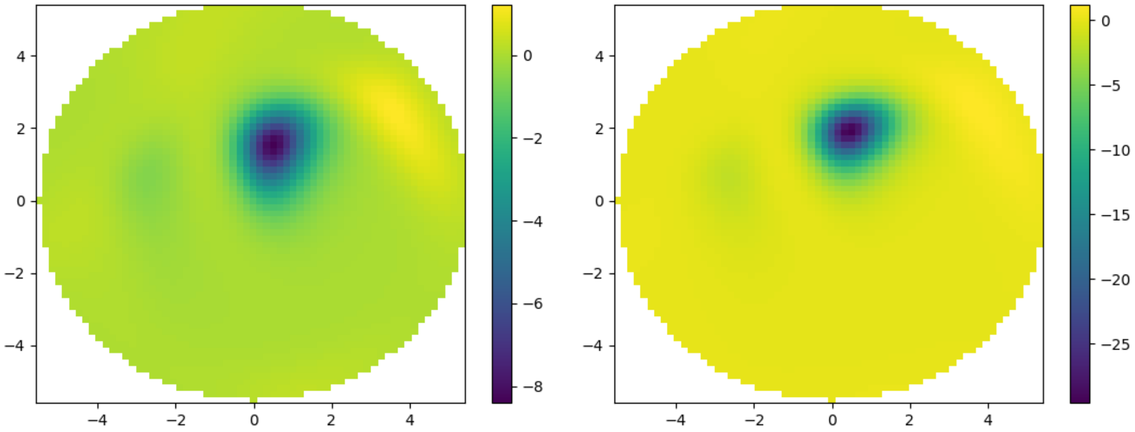

(a)

(b)

Figure 5.16: Glass Cup Top Imaging: (a) 1 kHz, (b) 10 kHz.

As in the previous test, the glass cup was correctly identified with a lower conductivity, as expected. It is also possible to observe that the artifact's size has slightly decreased, compared to when the glass cup was positioned on the left side, and, as this behavior was also observed during the tests with the bullet, it might be caused by the electrode problem previously mentioned. Nonetheless, the results obtained with the water tank are satisfactory, as it was possible to observe and correctly identify the change in relative conductivity in both cases.

5.2 Prototype comparison

Given the positive results obtained from the proposed prototype overall and when compared to the previously implemented prototype, Table 5.3 was developed to compare the two prototypes.

Table 5.3: Comparison between the two prototypes (as of September 2022).

	Proposed Prototype	**Previous Prototype**	**Notes**
Input Voltage	5 V	230 V	
Freq. Range	1 to 100 kHz	Unknown	
Electrode Capacity	32	12	
Current Amplitude	Fixed @ 500 µA	Inconsistent*	*Measured with a shunt resistor
Current Patterns	Adjacent, Opposite and User-Defined	Adjacent	
SNR Estimation	Yes	No	
Digital Filtering	Can be implemented	No	
Measurement	Differential and Single-Ended	Single-Ended	
Multiplexing	Solid State	Relay	
Cost	<150 €	>3000€	

When comparing the two prototypes, one characteristic stands out from all the others, the price. Using commercial sources, such as Mouser and RS Electronics, the proposed prototype presents a range of prices between 150 € and 170 €, most of it is composed of just the four multiplexing ICs and the Raspberry Pi Model 4. The previous prototype presents a typical price of 3500 € which is 20 times more than the proposed prototype.

Another highlighted feature of the proposed prototype is its ability to run on a 5 V power supply which, nowadays, most chargers can source. Using a Raspberry Pi also allows the implementation of digital processing blocks before any measurement is done on the signal (SNR Estimation, Digital Filtering, and so on...). All these features are impossible to implement with the previous prototype.

One feature the previous prototype implements better than the proposed prototype is the usage of relays instead of solid-state multiplexers. Since relays do not use any active element to switch the signals, their dynamic range is significantly greater and total harmonic distortion lower than most solid-state multiplexers present. However, one issue with this implementation is the size occupied by the relays, as it is possible to observe during the previous prototype presentation in Section 1.2, and the life span of such relays.

6

Conclusions

This Chapter presents the conclusions taken from all stages of this dissertation. These conclusions include the advantages and disadvantages of the proposed approach. The Chapter ends with a few suggestions for future work to improve the prototype developed during this dissertation.

6.1 Conclusions

Starting with the circuit development phase, most of the results obtained from the different module simulations were on par with real-life measurements done with multiple devices. Since all modules use ICs with SPICE models, it is possible to simulate and predict the entire system's behavior to an input. In a way, this makes the circuit development phase easier and increases confidence in the designed circuit.

One conclusion drawn from the software development phase is that, although the Raspberry Pi is pretty powerful, it lacks official support for many basic features, such as continuous SPI transfer with automatic chip select assortment. This fact, combined with constant interrupts caused by the Linux kernel, makes it impossible to obtain a fixed sampling frequency, making it unreliable for this project without using a second microcontroller to get the ADC's data.

Given the results obtained from the multiple tests done on the developed prototype, it is possible to draw a few conclusions. The first conclusion, given the results obtained from the Resistor Breakout Test, in Section 5.1.1, is that the ADC's precision and accuracy can be improved by using a low-noise reference IC different from the power supply reference. Some basic low-pass filtering can also help improve the ADC's performance. Another conclusion is that the ADC offset can be calibrated out of the system via software, reducing the absolute error but maintaining the standard deviation.

Overall, it is concluded that the system is working as intended since all the realized tests obtained their expected results, most importantly, the Breast Phantom test since this was the most realistic scenario available. Given this, the system is ready to be laid out on a single PCB, making it easier to use and removing any noise caused by using separate ground planes and floating wires, improving the measurements.

Since the prototype development is done in blocks and is fully documented, with the schematics, simulation results and PCB design, the improvement phase or feature adding is made much easier compared to the previous prototype, which uses proprietary material, making it impossible to add features. In the next Section, some improvements for the developed prototype are described to increase the system's accuracy and precision and even lower the material cost by using a standalone microcontroller instead of a Raspberry Pi.

6.2 Future Work

Switching from the Raspberry Pi Model 4B to a standalone microcontroller, such as the STM32H7 series, can bring multiple advantages since it includes a multiple channel, 16-bit ADC that can run up to 3.6 MSPS with automatic calibration, increasing the system's voltage and time resolution. Given its many ADC channels, measuring the injected signal through a shunt would make it possible to measure not only the output signal's amplitude but also its phase, allowing the calculation of both real and imaginary parts of the medium. This shunt would also increase the system's confidence by accurately measuring the injected current and signal distortion (caused by load limitations).

The STM32H7 series also includes a fast 12-bit DAC, with Direct Memory Access (DMA) off-load, running at 10 MSPS (using external components), which makes it possible to include the Signal Generation module directly on the microcontroller itself. This reduces the number of ICs and creates an almost pure analog board, removing high-speed SPI noise. Using a DAC also adds arbitrary waveform injection capabilities with variable amplitude, making the injected current value programmable instead of fixed.

Given the increase in the number of GPIOs, caused by removing both the SPI and the change in the microcontroller, lower amplification steps can be used by adding further amplification stages. This also allows the usage of lower gain but better PGAs, since the GBW is a limiting factor of these devices.

One final advantage of using the STM32H7 series over the Raspberry Pi is that the STM32H7 series presents two ARM processors, a Cortex-M7 running at 480 MHz and a Cortex-M4 running at 240 MHz [59], which greatly increases the performance of DSP-like applications. This way, one processor takes measurements while the other processes the data obtained, reducing the time between frames. The HALs typically used with Cortex processors, such as CMSIS [60], include multiple DSP-oriented functions optimized for the many Cortex processors available.

Bibliography

[1] DAQ970A/DAQ973A Data Acquisition System. https://www.keysight.com/us/en/assets/7018-06259/technical-overviews/5992-3168.pdf. Accessed: September 2022.

[2] DAQM900A 20 Channel Solid-state Multiplexer module. https://www.keysight.com/us/en/product/DAQM900A/20-channel-solid-state-multiplexer-module-for-daq970a-daq973a.html. Accessed: September 2022.

[3] Juliana Padilha Leitzke and Hubert Zangl. A review on electrical impedance tomography spectroscopy. Sensors, 20(18), 2020.

[4] IEC 60601-1:2015. Medical electrical equipment part 1: General requirements for basic safety and essential performance. Brussels: International Electrotechnical Commission, 2015.

[5] David Holder. Electrical impedance tomography: Methods, history, and applications. CRC Press, 2004.

[6] S.B. Ayati. A portable eit system for emergency medical care, Jan 2016.

[7] Fausto Andrés Escobar Revelo. Electrical impedance tomography: Hardware fundamentals and medical applications. Ingeniería Solidaria, 16(3), 2020.

[8] Zheng Zong, Yusong Wang, and Zhun Wei. A review of algorithms and hardware implementations in electrical impedance tomography (invited). Progress In Electromagnetics Research, 169:59–71, 2020.

[9] B H Brown, D C Barber, and A D Seagar. Applied potential tomography: possible clinical applications. Clinical Physics and Physiological Measurement, 6(2):109–121, 1985.

[10] F. J. McArdle, B. H. Brown, R. G. Pearse, and D. C. Barber. The effect of the skull of low-birthweight neonates on applied potential tomography imaging of centralised resistivity changes. Clinical Physics and Physiological Measurement, 9(4A):55–60, Nov 1988.

[11] A D Leathard, B H Brown, J Campbell, F Zhang, A H Morice, and D Tayler. A comparison of ventilatory and cardiac related changes in EIT images of normal human lungs and of lungs with pulmonary emboli. Physiological Measurement, 15(2A):A137–A146, May 1994.

[12] Anton Vonk Noordegraaf, Andre Janse, Pieter E. Postmus, Peter M.j.m. De Vries, Theo J.c. Faes, Johan T. Marcus, and Jean G.f. Bronzwaer. Noninvasive assessment of right ventricular diastolic function by electrical impedance tomography. Chest, 111(5):1222–1228, 1997.

[13] Henk J. Smit, Anton Vonk-Noordegraaf, J. Tim Marcus, Saskia Van Der Weijden, Pieter E. Postmus, Peter M.j.m. De Vries, and Anco Boonstra. Pulmonary Vascular Responses to Hypoxia and Hyperoxia in Healthy Volunteers and COPD Patients Measured by Electrical Impedance Tomographya. Chest, 123(6):1803–1809, 2003.

[14] B H Brown and A D Seagar. The sheffield data collection system. Clinical Physics and Physiological Measurement, 8(4A):91–97, Nov 1987.

[15] Eckhard Teschner, Michael Imhoff, and Steffen Leonhardt. Electrical Impedance Tomography: The realisation of regional ventilation Monitoring, 2nd edition. Dräger Medical GmbH, Jan 2015.

[16] A D Leathard, B H Brown, J Campbell, F Zhang, A H Morice, and D Tayler. A comparison of ventilatory and cardiac related changes in eit images of normal human lungs and of lungs with pulmonary emboli. Physiological Measurement, 15(2A), 1994.

[17] A J Wilson, P Milnes, A R Waterworth, R H Smallwood, and B H Brown. Mk3.5: a modular, multi-frequency successor to the mk3a eis/eit system. Physiological Measurement, 22(1):49–54, 2001.

[18] J. Hinz, A. Gehoff, O. Moerer, I. Frerichs, G. Hahn, G. Hellige, and M. Quintel. Regional filling characteristics of the lungs in mechanically ventilated patients with acute lung injury. European Journal of Anaesthesiology, 24(5):414–424, 2007.

[19] Inéz Frerichs, Peter A. Dargaville, Huibert Van Genderingen, Denis R. Morel, and Peter C. Rimensberger. Lung Volume Recruitment after Surfactant Administration Modifies Spatial Distribution of Ventilation. American Journal of Respiratory and Critical Care Medicine, 174(7):772–779, 2006.

[20] Martijn Miedema, Frans H. De Jongh, Inez Frerichs, Mariëtte B. Van Veenendaal, and Anton H. Van Kaam. Regional respiratory time constants during lung recruitment in high-frequency oscillatory ventilated preterm infants. Intensive Care Medicine, 38(2):294–299, 2011.

[21] Rebecca J. Yerworth, Inéz Frerichs, and Richard Bayford. Analysis and compensation for errors in electrical impedance tomography images and ventilation-related measures due to serial data collection. Journal of Clinical Monitoring and Computing, 31(5):1093–1101, 2016.

[22] Michelle M. Mellenthin, Jennifer L. Mueller, Erick Dario Leon Bueno De Camargo, Fernando Silva De Moura, Talles Batista Rattis Santos, Raul Gonzalez Lima, Sarah J. Hamilton, Peter A. Muller, and Melody Alsaker. The ace1 electrical impedance tomography system for thoracic imaging. IEEE Transactions on Instrumentation and Measurement, 68(9):3137–3150, 2019.

[23] Ji-Jer Huang, Yi-Hsuan Hung, Jhi-Joung Wang, and Bor-Shyh Lin. Design of wearable and wireless electrical impedance tomography system. Measurement, 78:9–17, 2016.

[24] Zhou Zhou, Nan Li, Hui Xu, Jin Guo, Zhaolin Sun, Haijun Liu, and Hongqi Yu. The Design and Implementation of a Portable EIT Telemedicine System. In 2012 Second International Conference on Intelligent System Design and Engineering Application, pages 571–575, 2012.

[25] Y Zou and Z Guo. A review of electrical impedance techniques for breast cancer detection. Medical engineering & physics, 25:79–90, Apr 2003.

[26] Eunjung Lee, Munkh-Erdene Ts, Jin Keun Seo, and Eung Je Woo. Breast EIT using a new projected image reconstruction method with multi-frequency measurements. Physiological Measurement, 33(5):751–765, Apr 2012.

[27] R.j. Halter, A. Hartov, and K.d. Paulsen. A Broadband High-Frequency Electrical Impedance Tomography System for Breast Imaging. IEEE Transactions on Biomedical Engineering, 55(2):650–659, 2008.

[28] Sunjoo Hong, Kwonjoon Lee, Unsoo Ha, Hyunki Kim, Yongsu Lee, Youchang Kim, and Hoi-Jun Yoo. A 4.9 mΩ-sensitivity mobile electrical impedance tomography ic for early breast-cancer detection system. IEEE Journal of Solid-State Circuits, 50(1):245–257, 2015.

[29] Yongsu Lee, Unsoo Ha, Kiseok Song, and Hoi-jun Yoo. 3.8 mw electrocardiogram (ecg) filtered electrical impedance tomography ic using i/q homodyne architecture for breast cancer diagnosis. In 2014 IEEE International Symposium on Circuits and Systems (ISCAS), pages 2389–2392, 2014.

[30] Hun Wi, Harsh Sohal, Alistair Lee McEwan, Eung Je Woo, and Tong In Oh. Multi-frequency electrical impedance tomography system with automatic self-calibration for long-term monitoring. IEEE Transactions on Biomedical Circuits and Systems, 8(1):119–128, 2014.

[31] Sunjoo Hong, Jaehyuk Lee, Joonsung Bae, and Hoi-Jun Yoo. A 10.4 mw electrical impedance tomography soc for portable real-time lung ventilation monitoring system. IEEE Journal of Solid-State Circuits, 50(11):2501–2512, 2015.

[32] R J Yerworth, R H Bayford, G Cusick, M Conway, and D S Holder. Design and performance of the uclh mark 1b 64 channel electrical impedance tomography (eit) system, optimized for imaging brain function. Physiological Measurement, 23(1):149–158, 2002.

[33] Tong In Oh, Eung Je Woo, and David Holder. Multi-frequency EIT system with radially symmetric architecture: KHU Mark1. Physiological Measurement, 28(7), 2007.

[34] Chao Tan, Shiwei Liu, Jiabin Jia, and Feng Dong. A wideband electrical impedance tomography system based on sensitive bioimpedance spectrum bandwidth. IEEE Transactions on Instrumentation and Measurement, 69(1):144–154, 2020.

[35] AD9837 Datasheet.
`https://www.analog.com/media/en/technical-documentation/data-sheets/ad9837.pdf`.
Accessed: April 2022.

[36] LM324PT Datasheet.
`https://eu.mouser.com/datasheet/2/389/cd00001046-1795623.pdf`.
Accessed: April 2022.

[37] LM324 Spice Model.
`https://github.com/pepaslabs/LTSpice-parts/blob/master/parts/op%20amp/LM324.ti.lib`.
Accessed: April 2022.

[38] NanoVNA Official Website.
`https://nanovna.com/`.
Accessed: December 2022.

[39] Xiaoke Li, Feng Dong, and Yan Fu. Analysis of constant-current characteristics for current sources. 2012 24th Chinese Control and Decision Conference (CCDC), 2012.

[40] Reza Ghorbani and Manoochehr Nahvi. Analysis of performance of howland ac current source for electrical impedance spectro-tomography. Sensing and Imaging, 20(1), 2019.

[41] Sergio Franco. Design with operational amplifiers and Analog Integrated Circuits. McGraw-Hill Education, 2015.

[42] Linden T. Harrison. Current sources & voltage references. Elsevier/Newnes, 2009.

[43] LTspice Simulator | Analog Devices.
`https://www.analog.com/en/design-center/design-tools-and-calculators/ltspice-simulator.html`.
Accessed: April 2022.

[44] LMH6624 Datasheet.
`https://www.ti.com/lit/ds/symlink/lmh6624.pdf`.
Accessed: April 2022.

[45] AD8099 Datasheet.
`https://eu.mouser.com/datasheet/2/609/AD8099-1502029.pdf`.
Accessed: April 2022.

[46] Andy Adler and David Holder. Electrical impedance tomography: Methods, history and applications. CRC Press, 2022.

[47] AD8253 Datasheet.
https://eu.mouser.com/datasheet/2/609/AD8253-1502348.pdf.
Accessed: April 2022.

[48] Ching Man. Quantization Noise: An Expanded Derivation of the Equation, SNR = 6.02 N + 1.76 dB, 2012.

[49] LTC2365 Datasheet.
https://www.analog.com/media/en/technical-documentation/data-sheets/23656fb.pdf.
Accessed: April 2022.

[50] Stuart Servis and Miguel U. Merino. Maximize the Performance of Your Sigma-Delta ADC Driver. Analog Dialogue, 53(05), May 2019.

[51] Rahul Kulkarni. Designing a Small-Size and Cost-Optimized Multi-Channel Data Acquisition System. Data Converter Products, June 2019.

[52] Piyu Dhaker. Introduction to SPI Interface. Analog Dialogue, 52(09), September 2018.

[53] bcm2835: C library for Broadcom 2835.
https://www.airspayce.com/mikem/bcm2835/.
Accessed: August 2022.

[54] Mihai Alexandru Ili, Pitică Dan, and Liviu Viman. Impedance meter based on iq demodulators. In 2018 41st International Spring Seminar on Electronics Technology (ISSE), pages 1–4, 2018.

[55] J L Mueller and S Siltanen. The d-bar method for electrical impedance tomography—demystified. Inverse Problems, 36(9):093001, sep 2020.

[56] Michael Schünke, Erik Schulte, Udo Schumacher, Jürgen Rude, Lawrence M Ross, Markus Voll, Karl Wesker, Terry C Telger, and Judith Tomat. General anatomy and musculoskeletal system. Thieme Medical Publishers, 2014.

[57] Siniša Sovilj, Ratko Magjarević, Amr Al Abed, Nigel H. Lovell, and Socrates Dokos. Simplified 2d bidomain model of whole heart electrical activity and ecg generation. Measurement Science Review, 14(3):136–143, 2014.

[58] Bárbara L Oliveira, Declan O'Loughlin, Martin O'Halloran, Emily Porter, Martin Glavin, and Edward Jones. Microwave breast imaging: experimental

tumour phantoms for the evaluation of new breast cancer diagnosis systems. Biomedical Physics & Engineering Express, 4(2):025036, feb 2018.

[59] STM32H7 - ARM Cortex-M7 and Cortex-M4 MCUs.
`https://www.st.com/en/microcontrollers-microprocessors/stm32h7-series.html`.
Accessed: August 2022.

[60] CMSIS - Arm Developer.
`https://developer.arm.com/tools-and-software/embedded/cmsis`.
Accessed: August 2022.

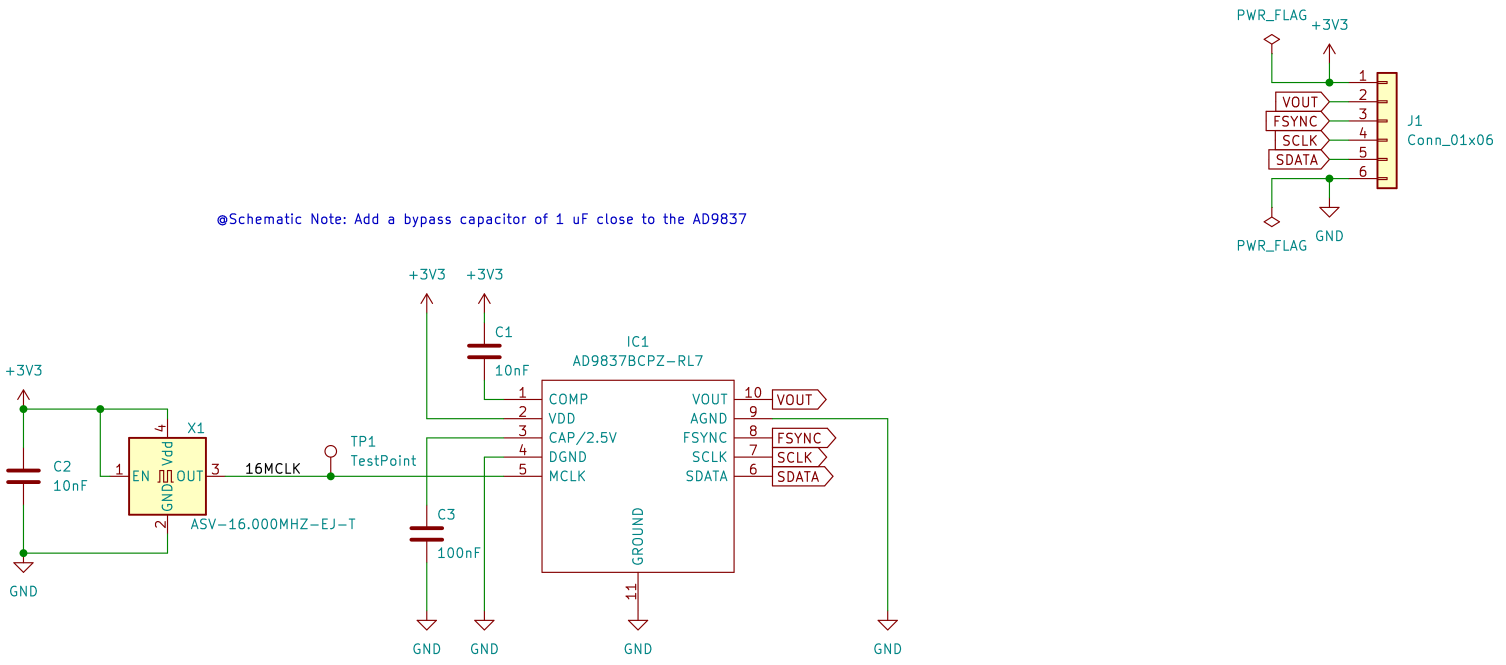

Fábio Silva

Sheet: /
File: SG.kicad_sch

Title: Signal Generator based on AD9837

Size: A4 Date: 2022-02-07 **Rev: 1.0**
KiCad E.D.A. kicad (6.0.1) Id: 1/1

@Assembly Note: Use 0.1% or lower resistors to avoid imbalances.

R1 = R4 + R5
R2 = R3

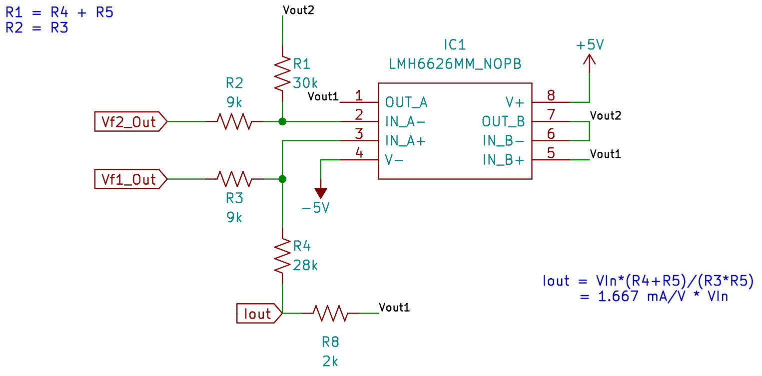

Iout = VIn*(R4+R5)/(R3*R5)
= 1.667 mA/V * VIn

Voltage Controlled Current Source (VCCS)

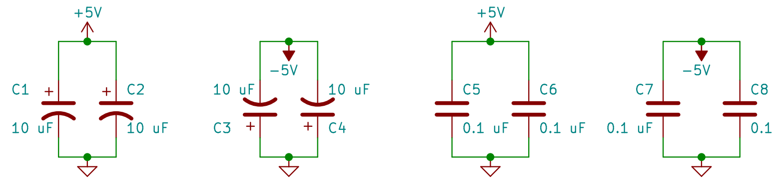

Supply/Bypass Capacitors

@Assembly Note: Use 0.1% or lower resistors to avoid imbalances.

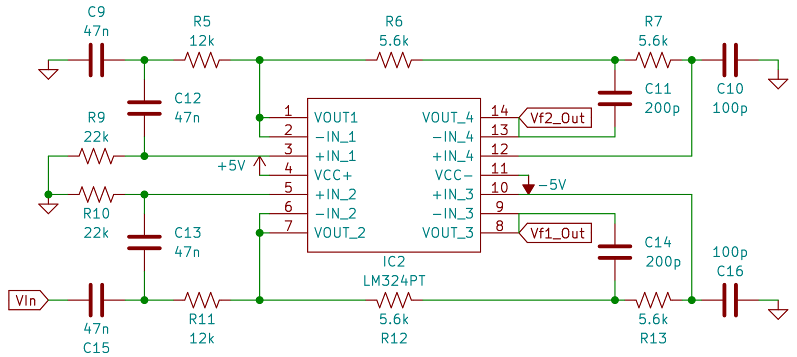

Band−Pass Filter based on Sallen−Key Topology

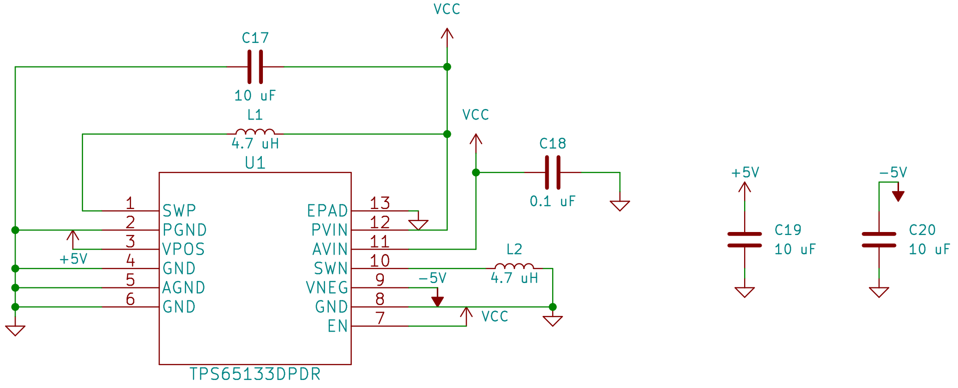

Split−Rail Power Supply (+5V/−5V)
Based on Typical Application from TPS65133 Datasheet

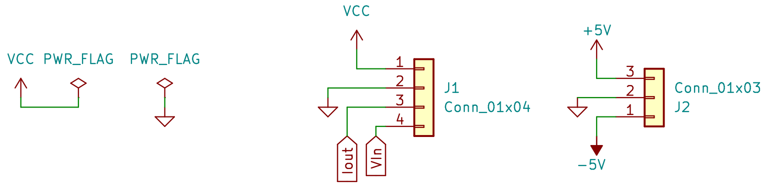

Connectors & Power Flags

Fábio Silva

Sheet: /
File: VCCS.kicad_sch

Title: Voltage Controlled Current Source based on LMH6626

Size: A4 Date: 2022−03−10 **Rev: 1.1**
KiCad E.D.A. kicad (6.0.1) Id: 1/1

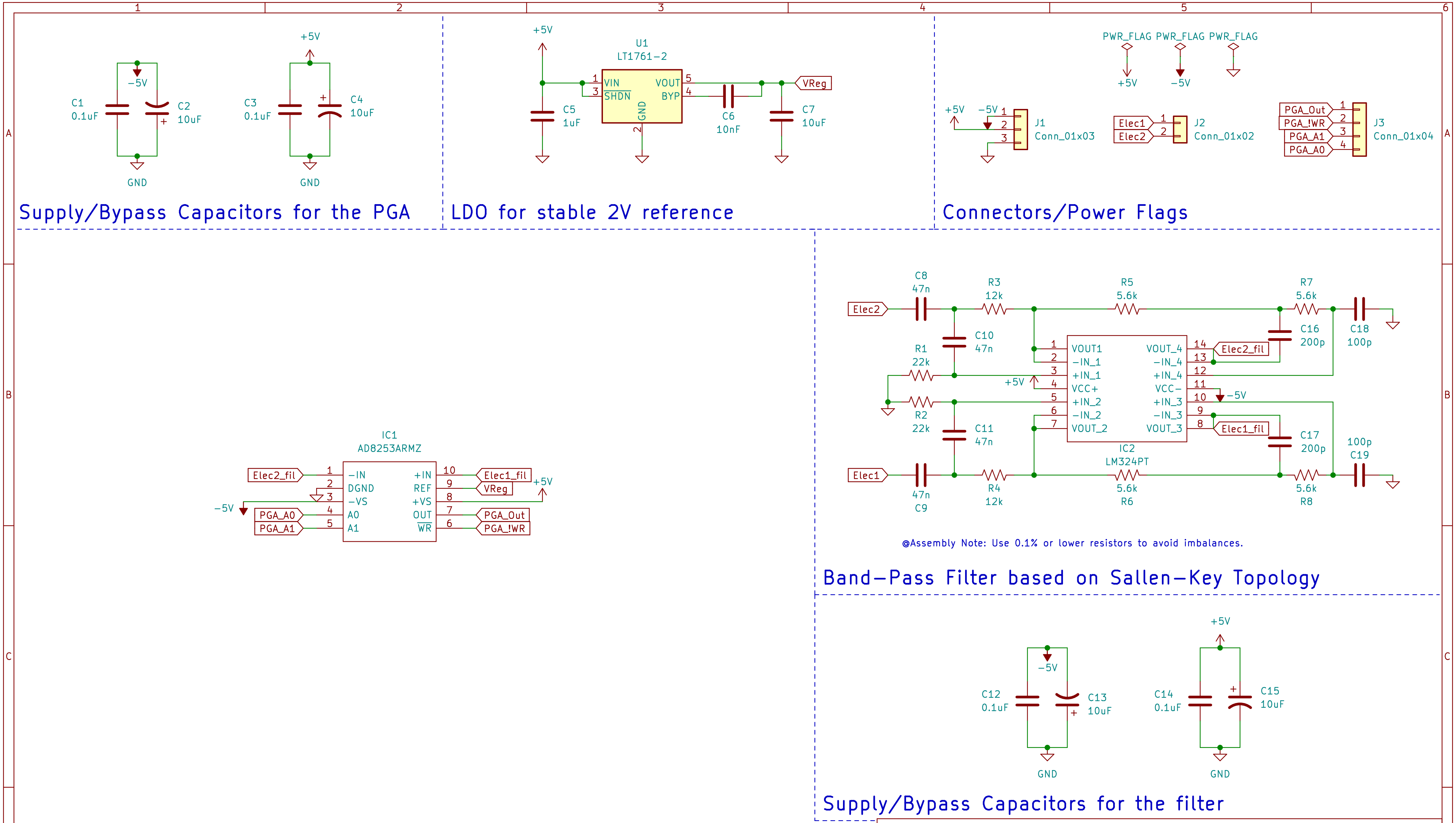

Fábio Silva

Sheet: /
File: PGA.kicad_sch

Title: PGA based on AD8253 with stable reference

Size: A4 Date: 2022-03-18 **Rev: v1**
KiCad E.D.A. kicad (6.0.1) Id: 1/1

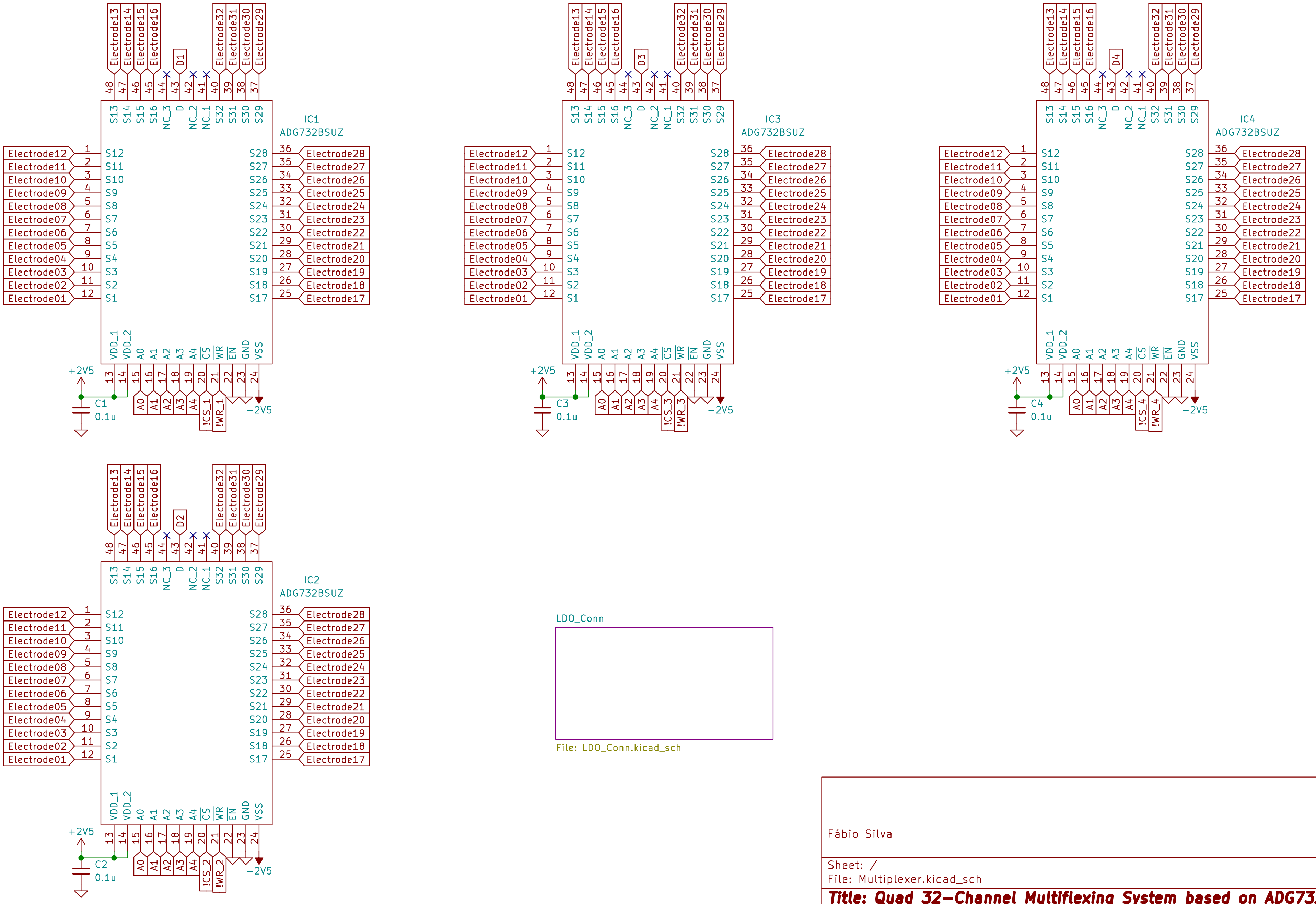

Fábio Silva

Sheet: /
File: Multiplexer.kicad_sch

Title: Quad 32-Channel Multiflexing System based on ADG732

Size: A4 Date: 2022-03-22 **Rev: v1**
KiCad E.D.A. kicad (6.0.1) Id: 1/2

@Schematic Note: Replace the ADP160 for an LM337 instead on the −2.5 V rail

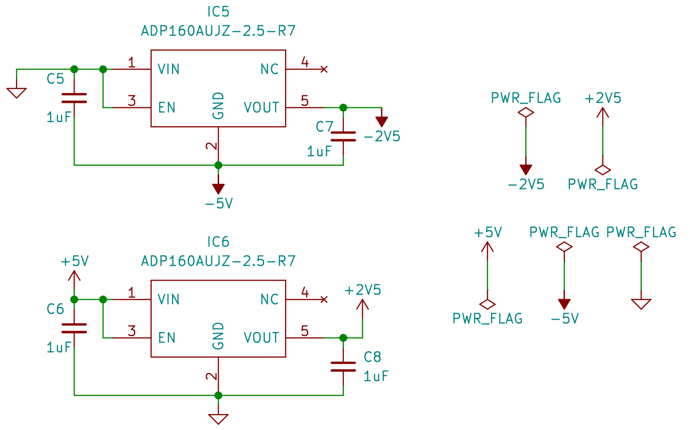

LDO Regulators for 2.5V Split−Rail + Power Flags

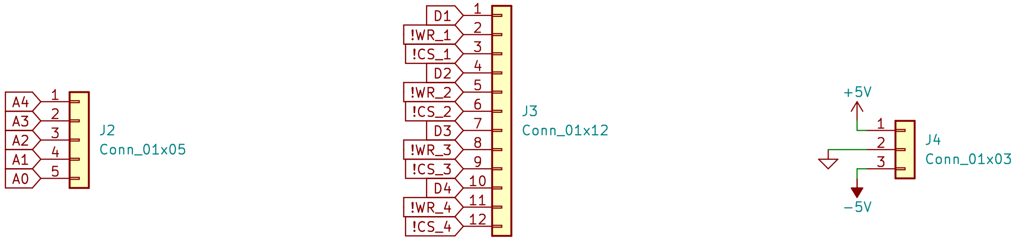

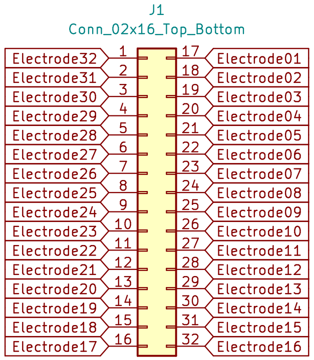

Electrode Connectors

NOTE: To facilitate PCB routing, the electrode connector was divided in two rows

Fábio Silva

Sheet: /LDO_Conn/
File: LDO_Conn.kicad_sch

Title: Multiplexer LDOs + Connectors

Size: A4 Date: 2022−03−22 **Rev: v1**
KiCad E.D.A. kicad (6.0.1) Id: 2/2

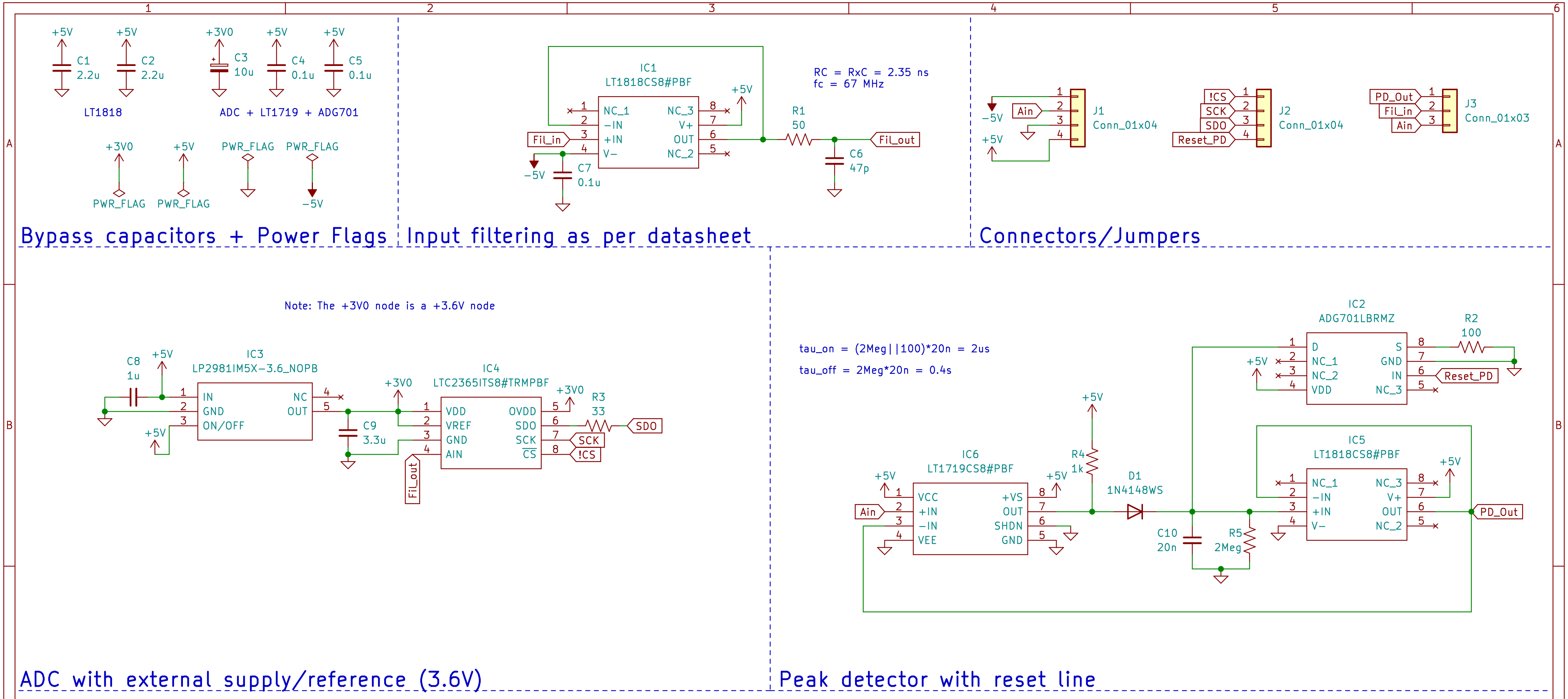

Fábio Silva

Sheet: /
File: ADC.kicad_sch

Title: 12-bit 1 MSPS ADC board based on the LTC2365

Size: A4
Date: 2022-04-01
Rev: v2
KiCad E.D.A. kicad (6.0.1)
Id: 1/1